

001  
002  
003  
004  
005

# Revisiting the zonally asymmetric extratropical circulation of the Southern Hemisphere spring using complex empirical orthogonal functions

006  
007  
008  
009  
010  
011  
012  
013  
014  
015  
016  
017  
018  
019  
020  
021  
022  
023  
024  
025  
026  
027  
028  
029  
030  
031  
032  
033  
034  
035  
036  
037  
038  
039  
040  
041  
042  
043  
044  
045  
046

Elio Campitelli<sup>1,2,3\*</sup>, Leandro B. Díaz<sup>1,2,3</sup> and Carolina  
Vera<sup>1,2,3</sup>

<sup>1</sup>\*Universidad de Buenos Aires, Facultad de Ciencias Exactas y  
Naturales, Departamento de Ciencias de la Atmósfera y los  
Océanos, Buenos Aires, Argentina.

<sup>2</sup>CONICET – Universidad de Buenos Aires. Centro de  
Investigaciones del Mar y la Atmósfera (CIMA), Buenos Aires,  
Argentina.

<sup>3</sup>CNRS – IRD – CONICET – UBA. Instituto Franco-Argentino  
para el Estudio del Clima y sus Impactos (IRL 3351 IFAECI),  
Buenos Aires, Argentina.

\*Corresponding author(s). E-mail(s):  
[elio.campitelli@cima.fcen.uba.ar](mailto:elio.campitelli@cima.fcen.uba.ar);

## Abstract

The large-scale extratropical circulation in the Southern Hemisphere is much more zonally symmetric than that of the Northern Hemisphere, but its zonal departures, albeit highly relevant for regional impacts, have been less studied. In this study we analyse the joint variability of the zonally asymmetric springtime stratospheric and tropospheric circulation using Complex Empirical Orthogonal Functions (cEOF) to characterise planetary waves of varying amplitude and phase. The leading cEOF represents variability of a zonal wave 1 in the stratosphere that correlates slightly with the Symmetric Southern Annular Mode (S-SAM). The second cEOF (cEOF2) is an alternative representation of the Pacific-South American modes. One phase of this cEOF is also

## 2 SH zonally asymmetric circulation with cEOF

047 very highly correlated with the Asymmetric SAM (A-SAM) in the tro-  
 048 posphere. Springs with an active ENSO tend to lock the cEOF2 to a  
 049 specific phase, but have no consistent impact on its magnitude. Fur-  
 050 thermore, we find indications that the location of Pacific Sea Surface  
 051 Temperature anomalies affect the phase of the cEOF2. As a result, the  
 052 methodology proposed in this study provides a deeper understanding  
 053 of the zonally asymmetric springtime extratropical SH circulation.

054 **Keywords:** Southern Hemisphere circulation, Teleconnections, Pacific South  
 055 American Mode, Southern Annular Mode, Stratosphere

## 059 1 Introduction

### introduction

060 The large-scale extratropical circulation in the Southern Hemisphere (SH) is  
 061 much more zonally symmetric than that of the Northern Hemisphere, but  
 062 departures from the zonal mean are associated with regional impacts (e.g.  
 063 [Hoskins and Hedges, 2005](#)). They strongly modulate weather systems and  
 064 regional climate through promoting longitudinally varying meridional trans-  
 065 port of heat, humidity, and momentum ([Trenberth, 1980](#); [Raphael, 2007](#)) and  
 066 could even be related to the occurrence of high-impact climate extremes ([Pezza](#)  
 067 [et al, 2012](#)).

068 The zonally asymmetric circulation is typically described by the amplitude  
 069 and phase of zonal waves obtained by Fourier decomposition of geopotential  
 070 height or sea-level pressure at each latitude (e.g. [van Loon and Jenne, 1972](#);  
 071 [Trenberth, 1980](#); [Turner et al, 2017](#)). This approach suggests that zonal waves  
 072 1 and 3 explain almost 99% of the total variance in the annual mean 500 hPa  
 073 geopotential height zonal anomalies at 50°S ([van Loon and Jenne, 1972](#)). [Tren-](#)  
 074 [berth and Mo \(1985\)](#) concluded that wave 3 plays a role in the development  
 075 of blocking events. In addition, previous works have identified wave-like pat-  
 076 terns with dominant wavenumbers 3-4 at extratropical and subpolar latitudes  
 077 with distinctive regional impacts. [Raphael \(2007\)](#) showed that variability in  
 078 the planetary wave 3 projected onto its climatological location is associated  
 079 with anomalies in the Antarctic sea-ice concentration.

080 Fourier decomposition relies on the assumption that the circulation can  
 081 be meaningfully described in terms of zonal waves of constant amplitude  
 082 along a latitude circle. However, this is not valid for meridionally propagating  
 083 waves or zonal waves with localised amplitudes. Addressing this limitation,  
 084 the Fourier technique can be generalized to integrate all planetary wave ampli-  
 085 tude regardless of wave number by computing the wave envelope ([Irving and](#)  
 086 [Simmonds, 2015](#)). The wave envelope can represent planetary waves with dif-  
 087 ferent amplitude at different longitudes, but lacks information about phase  
 088 and wave number. Using this method, [Irving and Simmonds \(2015\)](#) showed  
 089 that planetary wave amplitude in general is associated with Antarctic sea-ice

concentration and temperature, as well as to precipitation anomalies in regions of significant topography in SH mid-latitudes and Antarctica. 093  
094

Another extensively-used approach to characterise the SH tropospheric circulation anomalies, is computing Empirical Orthogonal Functions (EOF, also known as Principal Component Analysis). Within the EOF framework, the Southern Annular Mode (SAM) appears as the leading mode of variability 095  
096  
097  
098  
099  
100  
101  
102  
103  
104  
105  
106  
107  
108  
109  
110  
111  
112  
113  
114  
115  
of the SH circulation ([Fogt and Marshall, 2020](#)). Spatially, the SAM is characterised by a centre of geopotential anomalies over Antarctica surrounded by anomalies of the opposite sign at middle latitudes. Embedded in this zonally symmetric structure is a wave 3 pattern that is more prominent in the Pacific sector. The 2nd and 3rd EOFs, usually known as Pacific–South American Patterns (PSA) 1 and PSA2 patterns, respectively, describe meridionally propagating wave trains that originate in the eastern equatorial Pacific and Australian-Indian Ocean sector, and travel towards the South Atlantic following a great-circle arch along the Antarctic coast ([Mo and Paegle, 2001](#)). These patterns influence precipitation anomalies in South America ([Mo and Paegle, 2001](#)). Although these patterns are usually derived by applying EOF to temporal anomalies, [Raphael \(2003\)](#) also applied EOF methods specifically to zonal anomalies. [Irving and Simmonds \(2016\)](#) proposed a novel methodology for objectively identifying the PSA pattern using Fourier decomposition. More recently [Goyal et al \(2022\)](#) created an index of amplitude and phase of zonal wave 3-like variability by combining the two leading EOFs of meridional wind anomalies.

Some of the zonally asymmetric patterns of the SH circulation variability described previously appear to have experienced secular changes. For instance, [Raphael \(2003\)](#) suggests that the amplitude of the zonal wave 1 experienced a large increase and that the zonal wave 3 experienced changes in its annual cycle between 1958 and 1996. However, little is known yet about variability and trends of these patterns. 116  
117  
118  
119  
120  
121

Patterns resulting from EOF analysis are more flexible than Fourier decomposition-derived modes in that they can capture oscillation patterns that cannot be characterised by purely sinusoidal waves with constant amplitude. Nonetheless, they are restricted to standing oscillation modes and cannot properly represent propagating or phase-varying features such as zonal waves. A single EOF can also represent a mixture of two or more physical modes. 122  
123  
124  
125  
126  
127

A third methodology commonly used to describe circulation anomalies consists on identifying particular features of interest and creating indices using simple methods such as averages and differences. Examples of this methodology are the SAM Index of [Gong and Wang \(1999\)](#), the SH wave 3 activity index defined by [Raphael \(2004\)](#) and the SH zonally asymmetric circulation index from [Hobbs and Raphael \(2010\)](#). These derived methods are grounded on other methods such as Fourier decomposition or EOF to identify the centres of action for the described phenomena and can be useful to characterise features that are not readily apparent with these methods. These kinds of indices 128  
129  
130  
131  
132  
133  
134  
135  
136  
137  
138

#### 4 SH zonally asymmetric circulation with cEOF

139 are generally easy to compute, but they usually do not capture non-stationary  
 140 patterns.

141 An alternative methodology that has been proposed to study travelling  
 142 and standing waves is complex Empirical Orthogonal Functions (cEOF; [Horel](#)  
 143 ([1984](#))). This method extends EOF analysis to capture oscillations with vary-  
 144 ing amplitude and phase and has been applied to the time domain. For  
 145 instance, [Krokhin and Luxemburg \(2007\)](#) applied cEOF to station-based  
 146 monthly precipitation anomalies and monthly temperature anomalies in the  
 147 Eastern Siberia and the Far East region to characterise the main modes of vari-  
 148 ability and their relationship with teleconnection indices. Similarly, [Gelbrecht](#)  
 149 [et al \(2018\)](#) applied cEOF to daily precipitation from reanalysis to study the  
 150 propagating characteristics of the South American Monsoon. To our knowl-  
 151 edge, cEOF analysis has not been applied in the spatial domain to capture  
 152 the phase-varying nature of planetary waves in the atmosphere.

153 The general goal of this study is to improve the description and under-  
 154 standing of the zonally asymmetric extratropical SH circulation using cEOF,  
 155 which can describe phase varying planetary waves with variable amplitude  
 156 along a latitude circle. In addition, we try to expand the knowledge of the  
 157 simultaneous behaviour of SH asymmetric circulation in the troposphere and  
 158 the stratosphere.

159 We restrict this work to the September-October-November (SON)  
 160 trimester. During this season the tropical teleconnections over South America  
 161 are maximised ([Cazes-Boezio et al, 2003](#)), and the SH zonal winds associated  
 162 with the stratospheric polar vortex increase to peak in October and extend  
 163 downward after that ([Lim et al, 2018](#)).

164 In Section 2 we describe the methods. In Section 3.1 we analyse the spatial  
 165 patterns of each complex EOF. In Section 3.2 we study the spatial regressions  
 166 with geopotential height, temperature, and ozone anomalies. In Section 3.3 and  
 167 3.4 we analyse the relationship between cEOF2, the PSA and SAM modes. In  
 168 Section 3.5 we study tropical forcings that explain the variability of each cEOF.  
 169 In Section 3.6 we show the relationship between these modes of variability  
 170 and precipitation and surface temperature anomalies in South America and  
 171 Oceania. In Section 4 we compare our results with previous studies and discuss  
 172 the benefits of our methodology.

173

## 174 2 Data and Methods

175

methods

### 176 2.1 Data

177

data

178 We used monthly geopotential height, air temperature, ozone mixing ratio,  
 179 and total column ozone (TCO) at  $2.5^\circ$  longitude by  $2.5^\circ$  latitude of hori-  
 180 zontal resolution and 37 vertical isobaric levels from the European Centre for  
 181 Medium-Range Weather Forecasts Reanalysis version 5 [ERA; [Hersbach et al](#)  
 182 ([2019](#))] for the period 1979 – 2019. Most of our analysis is restricted to the  
 183 post-satellite era to avoid confounding factors arising from the incorporation  
 184 of satellite observations, but we also used the preliminary back extension of

ERA5 from 1950 to 1978 (Bell et al, 2020) to describe long-term trends. We derived streamfunction at 200 hPa from ERA5 vorticity using the FORTRAN subroutine FISHPACK (Adams et al, 1999) and we computed horizontal wave activity fluxes following Plumb (1985). Sea Surface Temperature (SST) monthly fields are from Extended Reconstructed Sea Surface Temperature (ERSST) v5 (Huang et al, 2017) and precipitation monthly data from the CPC Merged Analysis of Precipitation (CMAP, Xie and Arkin, 1997), with a 2° and 2.5° horizontal resolution, respectively. The rainfall gridded dataset is based on information from different sources such as rain gauge observations, satellite inferred estimations and the NCEP-NCAR reanalysis, and it is available from 1979 to the present.

The Oceanic Niño Index (ONI, Bamston et al, 1997) comes from NOAA's Climate Prediction Center and the Dipole Mode Index (DMI, Saji and Yamagata, 2003) from Global Climate Observing System Working Group on Surface Pressure.

## 2.2 Methods

The study is restricted to the spring season, defined as the September-October-November (SON) trimester. We compute seasonal means for the different variables, averaging monthly values weighted by the number of days in each month. We use the 200 hPa level to represent the upper troposphere and 50 hPa to represent the lower stratosphere.

We computed the amplitude and phase of the TCO wave 1 by averaging (area-weighted) the data of each SON between 75°S and 45°S, and then extracting the wave-1 component of the Fourier spectrum. We chose this latitude band because it is wide enough to capture most of the relevant anomalies of SH mid-latitudes.

We computed the level-dependent SAM index as the leading EOF of year-round monthly geopotential height anomalies south of 20°S at each level for the whole period (Baldwin and Thompson, 2009). We further split the SAM into its zonally symmetric and zonally asymmetric components (S-SAM and A-SAM indices respectively) following Campitelli et al (2022b). The method consists in first computing the leading EOF of monthly geopotential height anomalies at each level and then computing the zonal mean and the zonal anomalies from its spatial pattern. We then project each level's monthly geopotential height fields onto the corresponding EOF field, the zonally symmetric field and the zonally asymmetric fields to obtain time series corresponding to the full SAM, the symmetric SAM and the asymmetric SAM, respectively.

Seasonal indices of the PSA patterns (PSA1 and PSA2) were calculated, in agreement with Mo and Paegle (2001), as the third and fourth EOFs of seasonal mean anomalies for 500-hPa geopotential heights at SH.

Linear trends were computed by Ordinary Least Squares (OLS) and the 95% confidence interval was computed assuming a t-distribution with the appropriate residual degrees of freedom (Wilks, 2011).

6 *SH zonally asymmetric circulation with cEOF*

231  
232  
233  
234  
235  
236  
237  
238  
239  
240  
241  
242  
243  
244  
245  
246  
247  
248  
249  
250  
251  
252  
253  
254  
255  
256  
257  
258  
259  
260  
261  
262  
263  
264  
265  
266  
267  
268  
269  
270  
271  
272  
273  
274  
275  
276

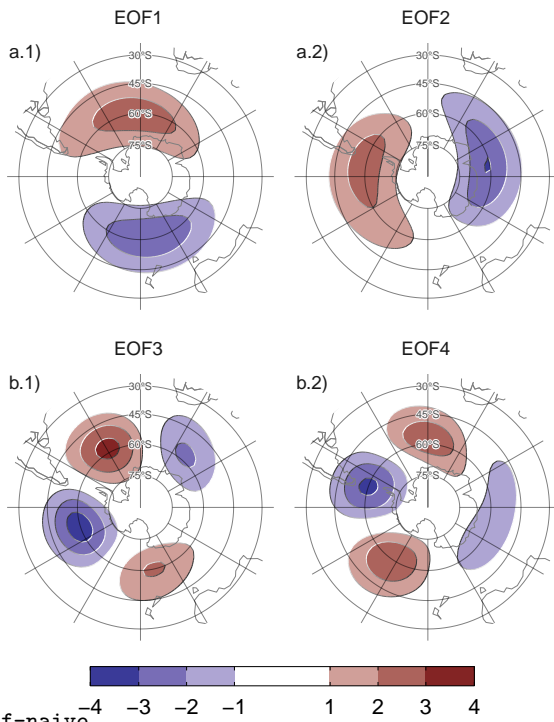


**Fig. 1:** Spatial patterns of the four leading EOFs of SON geopotential height zonal anomalies at 50 hPa south of 20° S for the 1979 – 2019 period (arbitrary units).

### 2.3 Complex Empirical Orthogonal Functions (cEOF)

ceof-methods

In the standard EOF analysis, zonal waves may appear as pairs of (possibly degenerate) EOFs representing similar patterns but shifted in phase (Horel, 1984). Figure 1 shows the four leading EOFs of SON geopotential height zonal anomalies at 50 hPa south of 20° S. It is clear that the first two EOFs represent a single phase-varying zonal wave 1 pattern and the last two represent a similarly phase-varying pattern with higher wavenumber and three centres of action shifted by 1/4 wavelength (90° in frequency space).

To describe the phase-varying nature of these two wave patterns, one way is to combine each pair of EOFs into indices of amplitude and phase. So, for instance, the amplitude of the wave 1-like EOF could be measured as  $\sqrt{PC1^2 + PC2^2}$  and its phase as  $\tan^{-1}(\frac{PC2}{PC1})$  (where PC1 and PC2 are the time series associated with each EOF). However, this rests on visual inspection of the spatial patterns and only works properly if both phases appear clearly in different EOFs, which is not guaranteed by construction. In particular, this does not work with the wave 1 pattern depicted as the leading EOF in 200 hPa geopotential height zonal anomalies (not shown).

On the other hand, a better alternative for describing phase-varying waves is to use Complex Empirical Orthogonal Functions (cEOF) analysis (Horel, 1984). Each cEOF is a set of complex-valued spatial patterns and time series. The real and imaginary components of the complex spatial pattern can be thought of as representing two spatial patterns that are shifted by 1/4 wavelength by construction, similar to EOF1 and EOF2 in Figure 1. In this paper we use the term 0° cEOF and 90° cEOF to refer to each part of the whole cEOF. The actual field reconstructed by each cEOF is then the linear combination of the two spatial fields weighted by its respective time series. This is analogous to how any sine wave can be constructed by the sum of a sine wave and cosine wave with different amplitude but constant phase. This means that cEOFs naturally represent phase-varying wave-like patterns that change location as well as amplitude.

For instance, when the phase of the wave matches the 0° phase, then the 0° phase time series is positive, and the 90° phase time series is zero. Similarly, when the phase of the wave matches the 90° phase, the 90° phase time series is positive, and the 0° phase time series is zero. The intermediate phases have non-zero values in both time series.

In traditional EOFs, the resulting modes are not unique, and instead are defined up to sign, which corresponds to a rotation in the complex plane of either 0 or  $\pi$ . In the same way, cEOFs are defined up to a rotation in the complex plane of any value between 0 and  $2\pi$  (Horel, 1984).

cEOFs are computed in the same way as traditional EOFs except that the data is first augmented by computing its analytic signal. This is a complex number whose real part is the original series and whose imaginary part is the original data shifted by 90° at each spectral frequency – i.e. its Hilbert transform. The Hilbert transform is usually understood in terms of time-varying signal. However, in this work we apply the Hilbert transform at each latitude circle, level, and at each SON mean (i.e. the signal only depends on longitude). Since each latitude circle is a periodic domain, this procedure does not suffer from edge effects.

We first applied cEOF analysis to geopotential height zonal anomalies south of 20°S at 50 and at 200 hPa. Figure 2 a.1 shows the spatial patterns of the two leading cEOF. The 0° phase is plotted with shaded contours and the 90° phase, with black contours. The two phases of the leading cEOF are very similar to the two leading EOFs shown in Figure 1 and represent a zonal wave 1 pattern; the 0° phase is roughly the EOF1 and the 90° phase is roughly the EOF2).

Table 1 shows the coefficient of determination between time series of the amplitude of each cEOF across levels. There is a high degree of correlation between the magnitude of the respective cEOF1 and cEOF2 at each level. The spatial patterns of the 50 hPa and 200 hPa cEOFs are also similar (not shown).

Both the spatial pattern similarity and the high temporal correlation of cEOFs computed at 50 hPa and 200 hPa suggest that these are, to a large extent, modes of joint variability. This motivates the decision of performing

8 *SH zonally asymmetric circulation with cEOF*

323 **Table 1:** `tab:corr-ceof-splitted`  
 324 Coefficient of determination ( $r^2$ ) between the time series of the  
 325 absolute magnitude of complex EOFs computed separately at 200 hPa and 50  
 326 hPa (p-values lower than 0.01 in bold).

	50 hPa				
	200 hPa	cEOF1	cEOF2	cEOF3	
		cEOF1	<b>0.29</b>	0.01	0.03
330	cEOF2	0.00	<b>0.59</b>	0.02	
331	cEOF3	0.00	0.00	0.01	

333 cEOF jointly between levels. Therefore cEOFs were computed using data from  
 334 both levels at the same time. In that sense each cEOF has a spatial component  
 335 that depends on longitude, latitude and level, and a temporal component that  
 336 depends only on time.

337 Because we are computing the cEOFs of zonal anomalies and not temporal  
 338 anomalies, the cEOFs need to account for the time-mean zonal anomalies.  
 339 These will tend to be represented by the leading cEOF, which therefore will  
 340 have a non-zero temporal mean.

341 As mentioned before, the choice of phases is arbitrary and equally valid.  
 342 But to make the interpretation easier, we chose the phase of each cEOF so  
 343 that either the  $0^\circ$  cEOF or the  $90^\circ$  cEOF is aligned with meaningful variables  
 344 in our analysis. This procedure does not create spurious correlations, it only  
 345 takes an existing relationship and aligns it with a specific phase.

346 Preliminary analysis showed that the first cEOF was closely related to the  
 347 zonal wave 1 of TCO and the second cEOF was closely related to ENSO.  
 348 Therefore, we chose the phase of cEOF1 so that the time series corresponding  
 349 to the  $0^\circ$  cEOF1 has the maximum correlation with the zonal wave 1 of TCO  
 350 between  $75^\circ\text{S}$  and  $45^\circ\text{S}$ . Similarly, we chose the phase of cEOF2 so that the  
 351 coefficient of determination between the ONI and the  $0^\circ$  cEOF2 is minimised,  
 352 which also nearly maximises the correlation with the  $90^\circ$  cEOF2.

353 In Section 3.6 we show regressions of precipitation and temperature asso-  
 354 ciated with intermediate phases. For those plots, we rotated the cEOFs by  $1/4$   
 355 wavelength by multiplying the complex time series by  $\cos(\pi/4) + i \sin(\pi/4)$   
 356 and computing the regression on those rotated timeseries.

357 While we compute these complex principal components using data from  
 358 1979 to 2019, we extended the complex time series back to the 1950 – 1978  
 359 period by projecting monthly geopotential height zonal anomalies standardised  
 360 by level south of  $20^\circ\text{S}$  onto the corresponding spatial patterns.

361 We performed linear regressions to quantify the association between the  
 362 cEOFs and other variables (e.g. geopotential height, temperature, precipita-  
 363 tion, and others). For each cEOF, we computed regression maps by fitting a  
 364 multiple linear model involving both the  $0^\circ$  and the  $90^\circ$  phases. To obtain the  
 365 linear coefficients of a variable  $X$  with the  $0^\circ$  and  $90^\circ$  phase of each cEOF we  
 366 fit the equation

367

	369
	370
$X(\lambda, \phi, t) = \alpha(\lambda, \phi) \text{cEOF}_{0^\circ} + \beta(\lambda, \phi) \text{cEOF}_{90^\circ} + X_0(\lambda, \phi) + \epsilon(\lambda, \phi, t)$	371
	372

where  $\lambda$  and  $\phi$  are the longitude and latitude,  $t$  is the time,  $\alpha$  and  $\beta$  are the linear regression coefficients for  $0^\circ$  and  $90^\circ$  phases respectively,  $X_0$  and  $\epsilon$  are the constant and error terms respectively.

We evaluated statistical significance using a two-sided t-test and, in the case of regression maps, p-values were adjusted by controlling for the False Discovery Rate (Benjamini and Hochberg, 1995; Wilks, 2016) to avoid misleading results from the high number of regressions (Walker, 1914; Katz and Brown, 1991).

## 2.4 Computation procedures

We performed all analysis in this paper using the R programming language (R Core Team, 2020), using data.table (Dowle and Srinivasan, 2020) and metR (Campitelli, 2020) packages. All graphics are made using ggplot2 (Wickham, 2009). We downloaded data from reanalysis using the ecmwfr package (Hufkens, 2020) and indices of ENSO and Indian Ocean Dipole (IOD) with the rsoi package (Albers and Campitelli, 2020). The paper was rendered using knitr and rmarkdown (Xie, 2015; Allaire et al, 2020).

## 3 Results

### 3.1 cEOF spatial patterns

To describe the variability of the circulation zonal anomalies, the spatial and temporal parts of the first two leading cEOFs of zonal anomalies of geopotential height at 50 hPa and 200 hPa, computed jointly at both levels, are shown in Figures 2 and 3. The first mode (cEOF1) explains 82% of the variance of the zonally anomalous fields, while the second mode (cEOF2) explains a smaller fraction (7%). In the spatial patterns (Fig. 2), the  $0^\circ$  and the  $90^\circ$  phases are in quadrature by construction, so that each cEOF describe a single wave-like pattern whose amplitude and position (i.e. phase) is controlled by the magnitude and phase of the temporal cEOF. The wave patterns described by these cEOFs match the patterns seen in the standard EOFs of Figure 1.

The cEOF1 (Fig. 2 column 1) is a hemispheric wave 1 pattern with maximum amplitude at high latitudes. At 50 hPa the  $0^\circ$  cEOF1 has the maximum of the wave 1 at  $150^\circ\text{E}$  and at 200 hPa, the maximum is located at around  $175^\circ\text{E}$  indicating a westward shift with height. The cEOF2 (Fig. 1 column 2) shows also a zonal wave-like structure with maximum amplitude at high latitudes, but with shorter spatial scales. In particular, the dominant structure at both levels is a wave 3 but with larger amplitude in the pacific sector. There is no apparent phase shift with height but the amplitude of the pattern is greatly reduced in the stratosphere, which is consistent with the the fact that

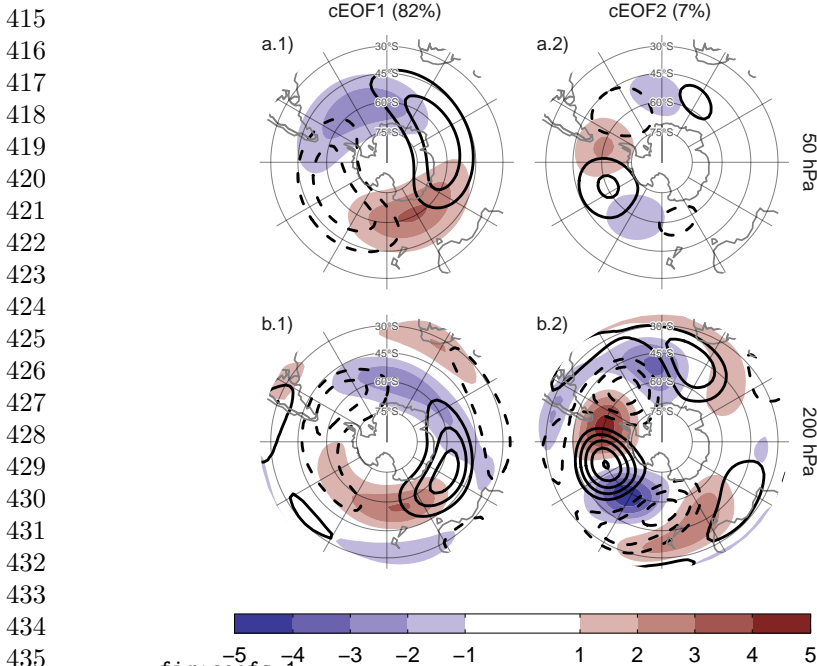


**Fig. 2:** Spatial patterns for the two leading cEOFs of SON geopotential height zonal anomalies at 50 hPa and 200 hPa for the 1979 – 2019 period. The shading (contours) corresponds to 0° (90°) phase. Arbitrary units. The proportion of variance explained for each mode with respect to the zonal mean is indicated in parenthesis.

the cEOF2 computed separately for 200 hPa explains a bit more variance than the cEOF2 computed separately for 50 hPa (11% vs. 3%, respectively). This suggest that this barotropic mode represents mainly tropospheric variability.

There is no significant simultaneous correlation between cEOFs time series. Both cEOFs show year-to-year variability but show no evidence of decadal variability (Fig. 3). The 0° cEOF has a non-zero temporal mean which, as discussed in Section 2.3, is due to the fact that the temporal mean of zonal anomalies need to be captured by the cEOFs. The other indices have almost zero temporal mean, which indicates that only cEOF1 includes variability that significantly projects onto the mean zonal anomalies. This is consistent with the fact that the mean zonal anomalies of geopotential height are very similar to the cEOF1 ( $r^2 = 98\%$ ) and not similar to the cEOF2 ( $r^2 = 0\%$ ).

A significant positive trend in the 0° phase of cEOF1 is evident (Fig. 3a.1, p-value = 0.0037) while there is no significant trend in any of the phases of cEOF2. The positive trend in the 0° cEOF1 translates into a positive trend in cEOF1 magnitude, but not systematic change in phase (not shown). This long-term change indicates an increase in the magnitude of the high latitude zonal wave 1.

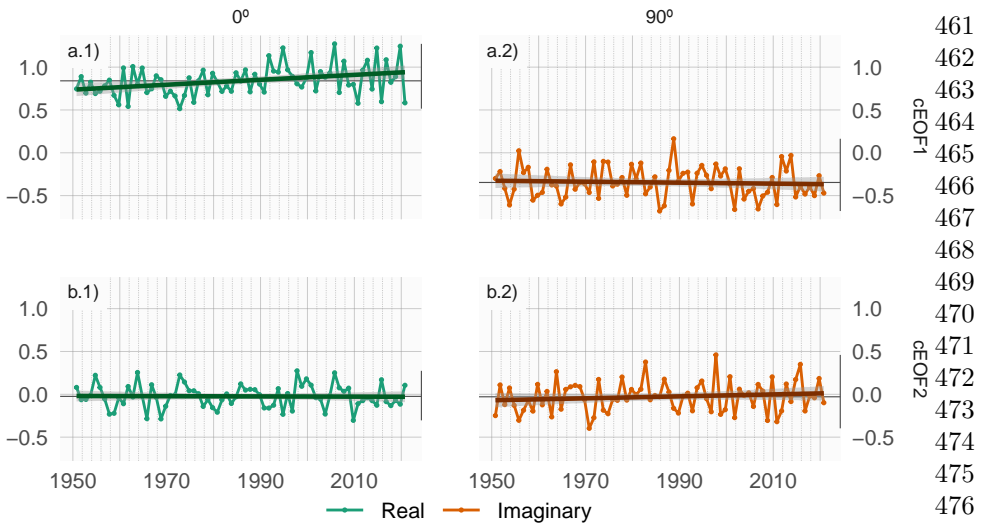


**Fig. 3:** Time series of the two leading cEOFs of SON geopotential height zonal anomalies at 50 hPa and 200 hPa. cEOF1 (row a) and cEOF2 (row b) separated in their 0° (column 1) and 90° (column 2) phase. Dark straight line is the linear trend. Black horizontal and vertical line mark the mean value and range of each time series, respectively.

fig:extended-series

## 3.2 cEOFs Regression maps

### 3.2.1 Geopotential

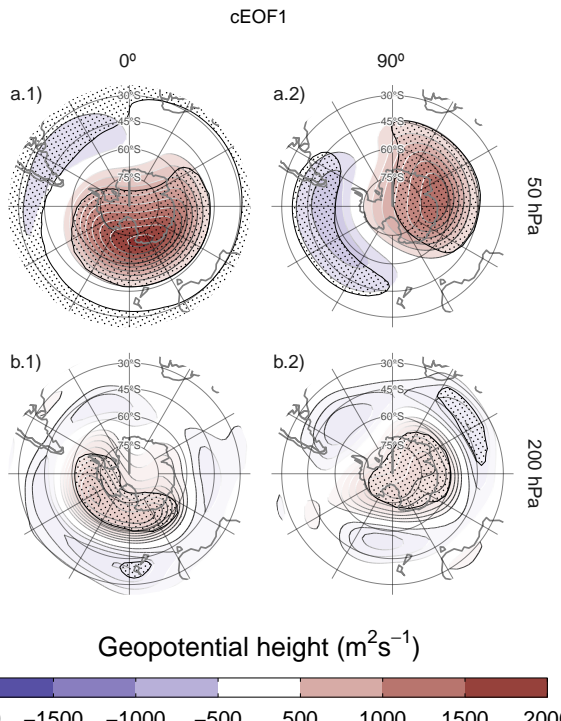
In the previous section, cEOF analysis was applied to zonal anomalies derived by removing the zonally mean values in order to isolate the main characteristics of the main zonal waves characterizing the circulation in the SH. In this section we compute regression fields using the full fields of the variables in order to describe the influence of the cEOFs on the temporal anomalies.

Figure 4 shows regression maps of SON geopotential height anomalies upon cEOF1. At 50 hPa (Figure 4 row a), the 0° cEOF1 is associated with a positive centre located over the Ross Sea. The correlation between the 0° cEOF1 and the zonal mean zonal wind at 60°S and 10hPa is -0.59 (CI: -0.76 – -0.35), indicating a moderate relationship with the SON stratospheric jet. The 90° cEOF1 is associated with a distinctive wave 1 pattern with maximum over the coast of East Antarctica. At 200 hPa (Figure 4 row b) the 0° cEOF1 shows a single centre of positive anomalies spanning West Antarctica surrounded by opposite anomalies in lower latitudes, with its centre shifted slightly eastward compared with the upper-level anomalies. The 90° cEOF1 shows a much more zonally symmetrical pattern resembling the negative SAM phase (e.g. [Fogt and Marshall, 2020](#)). Therefore, the magnitude and phase of the cEOF1 are associated with the magnitude and phase of a zonal wave mainly in the stratosphere.

regressions

geopotential

461  
462  
463  
464  
465  
466  
467  
468  
469  
470  
471  
472  
473  
474  
475  
476  
477  
478  
479  
480  
481  
482  
483  
484  
485  
486  
487  
488  
489  
490  
491  
492  
493  
494  
495  
496  
497  
498  
499  
500  
501  
502  
503  
504  
505  
506



**Fig. 4:** Regression of SON geopotential height anomalies ( $m^2 s^{-1}$ ) with the (column 1)  $0^\circ$  and (column 2)  $90^\circ$  phases of the first cEOF for the 1979 – 2019 period at (row a) 50 hPa and (row b) 200 hPa. These coefficients come from multiple linear regression involving the  $0^\circ$  and  $90^\circ$  phases. Areas marked with dots have p-values smaller than 0.01 adjusted for False Detection Rate.

Figure 5 shows the regression maps of geopotential height anomalies upon the cEOF2. In the troposphere (Fig. 5 row a) the regression maps show wave trains similar to those identified for cEOF2 patterns (Fig 2). Regressed anomalies associated with the  $0^\circ$  cEOF2 are  $1/4$  wavelength out of phase with those associated with the  $90^\circ$  cEOF2. All fields have a dominant zonal wave 3 limited to the western hemisphere, over the Pacific and Atlantic Oceans. cEOF2 then represents an equivalent barotropic wave train that is very similar to the PSA Patterns ([Mo and Paegle, 2001](#)). Comparing the location of the positive anomaly near  $90^\circ\text{W}$  in column 2 of Figure 5 with Figures 1.a and b from [Mo and Paegle \(2001\)](#), the  $0^\circ$  cEOF2 regression map could be identified with PSA2, while the  $90^\circ$  cEOF2 resembles PSA1.

These wave patterns are also present in the stratosphere (Fig. 5 row a) supporting their equivalent barotropic nature. But also present is a monopole over the pole with negative sign associated with the  $0^\circ$  cEOF2 and positive sign associated with the  $90^\circ$  cEOF2. This monopole might indicate strengthening of the polar vortex associated with positive values of the  $0^\circ$  cEOF2 and weakening

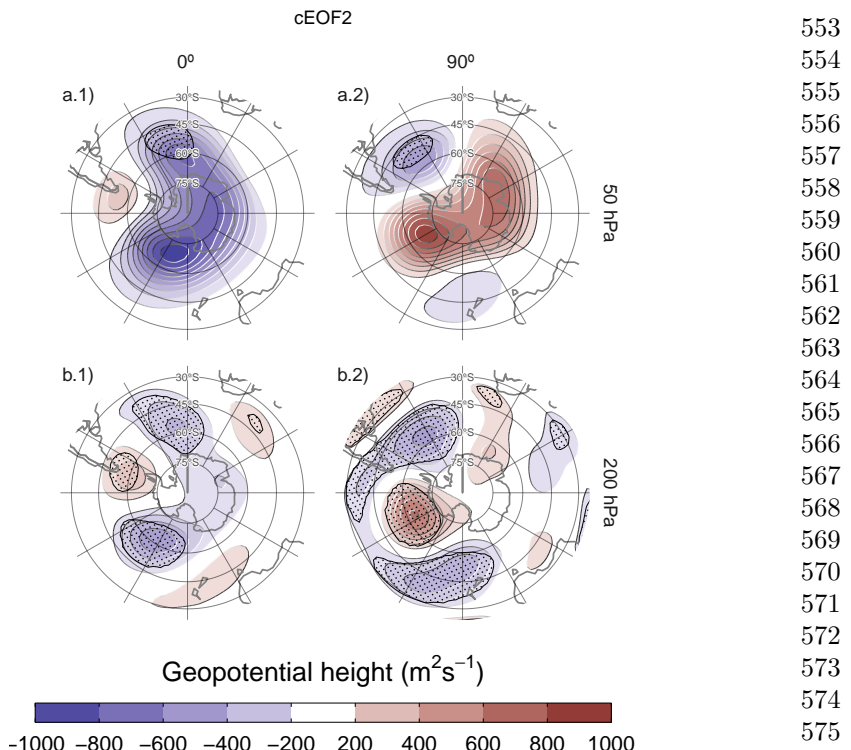


**Fig. 5:** Same as Figure 4 but for cEOF2.

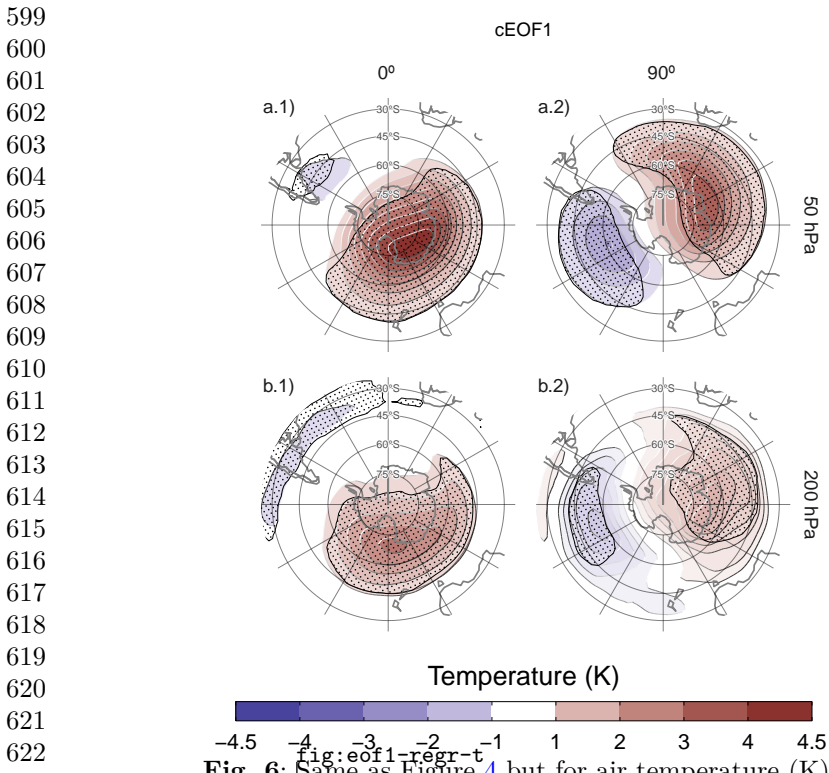
associated with negative values of 0° cEOF2. However, since these anomalies are not statistically significant, this feature should not be overinterpreted.

### 3.2.2 Temperature and Ozone

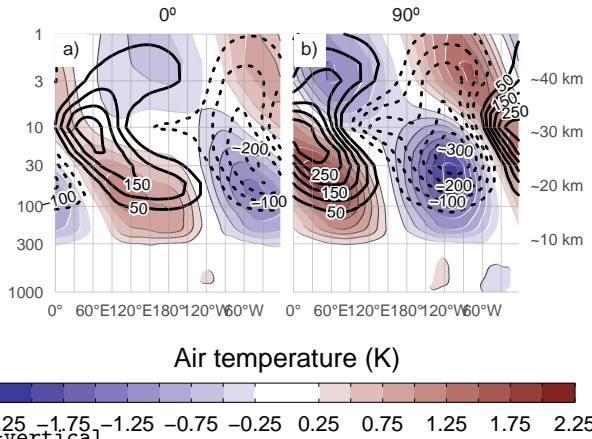
The signature of cEOFs variability on air temperature was also evaluated. Figure 6 shows regression maps of air temperature anomalies at 50 hPa and 200 hPa upon cEOF1. The distribution of temperature regression coefficients at 50 hPa and at 200 hPa mirror the geopotential height regression maps at 50 hPa (Fig. 4). In both levels, the 0° cEOF1 is associated with a positive centre over the South Pole with its centre moved slightly towards 150°E (Fig. 6 column 1). On the other hand, the regression maps on the 90° cEOF1 show a clearer wave 1 pattern with its maximum around 60°E.

Figure 7 shows the vertical distribution of the regression coefficients on cEOF1 from zonal anomalies of air temperature and of ozone mixing ratio averaged between 75°S and 45°S. Temperature zonal anomalies associated with cEOF1 show a clear wave 1 pattern for both 0° and 90° phases throughout the atmosphere above 250 hPa with a sign reversal above 10 hPa. As a result of the hydrostatic balance, this is the level in which the geopotential anomaly have maximum amplitude (not shown).

temp-ozone  
582  
583  
584  
585  
586  
587  
588  
589  
590  
591  
592  
593  
594  
595  
596  
597  
598



**Fig. 6:** Same as Figure 4 but for air temperature (K).



**Fig. 7:** Regression of SON zonal anomalies averaged between 75°S and 45°S of mean air temperature (shaded, Kelvin) and ozone mixing ratio (contours, negative contours with dashed lines, labels in parts per billion by mass) with the (a) 0° and (b) 90° phase of the cEOF1 for the 1979 – 2019 period.

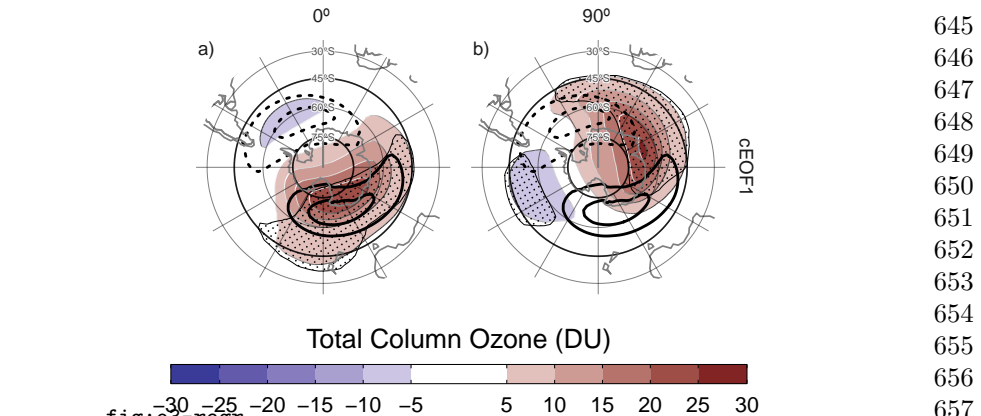


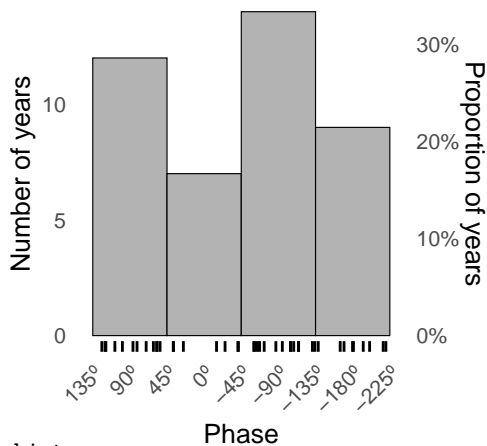
**Fig. 8:** Regression of SON mean Total Column Ozone anomalies (shaded, Dobson Units) with the (a)  $0^\circ$  and (b)  $90^\circ$  phases of the cEOF1 for the 1979–2019 period. On contours, the mean zonal anomaly of Total Column Ozone (negative contours in dashed lines, Dobson Units). Areas marked with dots have p-values smaller than 0.01 adjusted for False Detection Rate.

The maximum ozone regressed anomalies coincide with the minimum temperature anomalies above 10 hPa and with the maximum temperature anomalies below 10 hPa (Fig. 7). Therefore, the ozone zonal wave 1 is negatively correlated with the temperature zonal wave 1 in the upper stratosphere, and positively correlated in the upper stratosphere. This change in phase is observed in ozone anomalies forced by planetary waves that reach the stratosphere. In the photochemically-dominated upper stratosphere, cold temperatures inhibit the destruction of ozone, explaining the opposite behaviour for both variables as were elucidated with dynamical chemical models (Hartmann and Garcia, 1979; Wirth, 1993; Smith, 1995). On the other hand, in the advectively-dominated lower stratosphere, ozone anomalies are 1/4 wavelength out of phase with horizontal and vertical transport, which are in addition 1/4 wavelength out of phase with temperature anomalies, resulting in same sign anomalies for the response of both variables (Hartmann and Garcia, 1979; Wirth, 1993; Smith, 1995).

The regression maps of TCO anomalies upon cEOF1 (Fig. 8) show zonal wave 1 patterns associated with both components of cEOF1. The climatological position of the springtime Ozone minimum (ozone hole) is outside the South Pole and towards the Weddell Sea (e.g. Grytsai, 2011). Thus, the  $0^\circ$  cEOF1 regression field (Figure 8a) coincides with the climatological position of the ozone hole, while it is  $90^\circ$  out of phase for the  $90^\circ$  cEOF1. The temporal correlation between the amplitudes of TCO planetary wave 1 and the amplitude of cEOF1 is 0.79 (CI: 0.63 – 0.88), while the correlation between their phases is -0.85 (CI: -0.92 – -0.74). Consequently, cEOF1 is strongly related with the SH ozone variability.

691 **Table 2:** Correlation coefficients ( $r$ ) between cEOF2 components and the  
 692 PSA1 and PSA2 modes computed as Mo and Paegle (2001) for the 1979 –  
 693 2019 period. 95% confidence intervals in parenthesis. p-values lower than 0.01  
 694 in bold.

PC	cEOF2	
	Real	Imaginary
PSA1	0.26 (CI: -0.04 – 0.52)	<b>0.82 (CI: 0.69 – 0.9)</b>
PSA2	<b>0.79 (CI: 0.63 – 0.88)</b>	-0.02 (CI: -0.32 – 0.29)



702 **Fig. 9:** `fig:phase-histogram`  
 703 Histogram of phase distribution of cEOF2 phase for the 1979 – 2019  
 704 period. Bins are centred at 90°, 0°, -90°, -180° with a binwidth of 90°. The  
 705 small vertical lines near the horizontal axis mark the observations.  
 706

### 707 3.3 PSA

708 Given the similarity between the cEOF2 related-associated structures (Fig. 5)  
 709 and documented PSA patterns, we study the relationship between them.  
 710 Table 2 shows the correlations between the two PSA indices and the time series  
 711 for 0° and 90° phases of cEOF2. As visually anticipated by Figure 5, there is a  
 712 large positive correlation between PSA1 and 90° cEOF2, and between PSA2  
 713 and 0° cEOF2. On the other hand, there is no significant relationship between  
 714 PSA1 and 0° cEOF2, and between PSA2 and 90° cEOF2. As a result, cEOF2  
 715 represents well both the spatial structure and temporal evolution of the PSA  
 716 modes, so it is possible to make an association between its two phases and the  
 717 two PSA modes. That is, the phase election for cEOF2 that maximises the  
 718 relationship between ENSO and 90° cEOF2, also maximises the association  
 719 between cEOF2 components and PSA modes (not shown).

psa

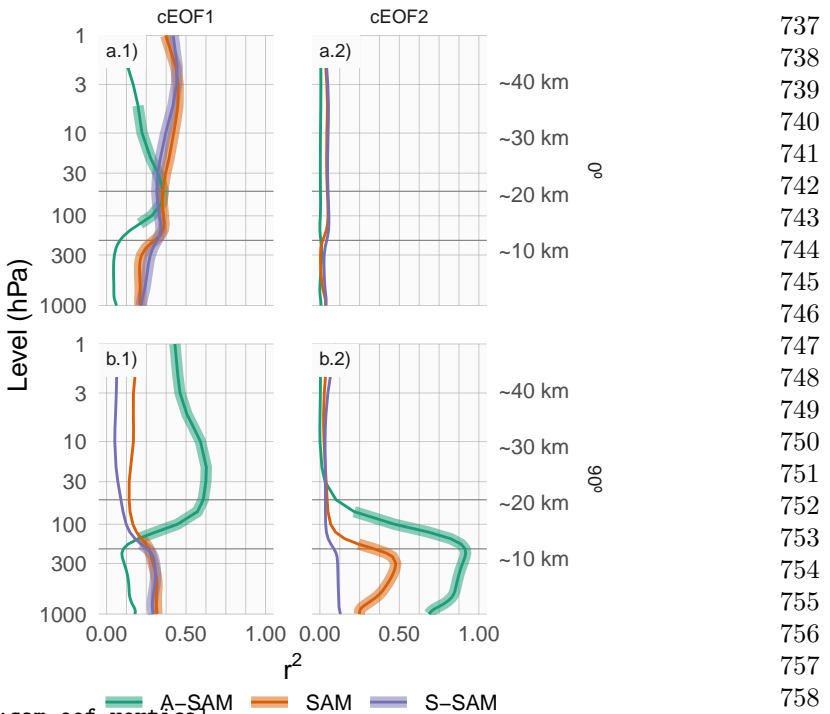


**Fig. 10:** fig:sam\_eof\_vertical Coefficient of determination ( $r^2$ ) between each component of cEOFs and the SAM, Asymmetric SAM (A-SAM) and Symmetric SAM (S-SAM) indices computed at each level for the 1979 – 2019 period. Thick lines represent estimates with  $p < 0.01$  corrected for False Detection Rate (Benjamini and Hochberg, 1995).

Figure 9 shows an histogram that counts the number of SON seasons in which the cEOF2 phase was close to each of the four particular phases (positive/negative of  $0^\circ$  and  $90^\circ$  phases), with the observations for each season marked as rugs on the horizontal axis. In 62% of seasons cEOF2 has a phase similar to either the negative or positive  $90^\circ$  phase, making the  $90^\circ$  phase the most common phase. This is also the phase that is most correlated with ENSO by the definition of the  $0^\circ$  phase as described in Section 2.

Therefore, by virtue of being the most common phase, the  $90^\circ$  cEOF2 explains more variance than the  $0^\circ$  cEOF2. Conventional EOF analysis will therefore tend to separate them relatively cleanly, with the EOF representing the  $90^\circ$  cEOF2 always leading the one representing the  $0^\circ$  cEOF2. This phase preference is in agreement with Irving and Simmonds (2016), who found a bimodal distribution to PSA-like variability (compare our Figure 9 with their Figure 6).

737  
738  
739  
740  
741  
742  
743  
744  
745  
746  
747  
748  
749  
750  
751  
752  
753  
754  
755  
756  
757  
758  
759  
760  
761  
762  
763  
764  
765  
766  
767  
768  
769  
770  
771  
772  
773  
774  
775  
776  
777  
778  
779  
780  
781  
782

783 **3.4 SAM**<sup>sam</sup>

784 We now explore the relationship between SAM and the cEOFs motivated by  
 785 the resemblance between cEOFs regression maps and SAM patterns shown in  
 786 Section 3.2. We computed the coefficient of determination between the cEOFs  
 787 time series and the three SAM indices (SAM, A-SAM and S-SAM) defined  
 788 by Campitelli et al (2022b) at each vertical level (Fig. 10). The SAM index  
 789 is statistically significantly correlated with the 0° cEOF1 in all levels, and  
 790 with the 90° cEOF1 and 90° cEOF2 in the troposphere. On the other hand,  
 791 correlations between SAM and the 0° cEOF2 are non-significant.

792 The relationship between the SAM and cEOF1 in the troposphere is  
 793 explained entirely by the zonally symmetric component of the SAM as shown  
 794 by the high correlation with the S-SAM below 100 hPa and the low and sta-  
 795 tistically non-significant correlations between the A-SAM and either the 0°  
 796 or 90° cEOF1. In the stratosphere, the 0° cEOF1 is correlated with both A-  
 797 SAM and S-SAM, while the 90° cEOF1 is highly correlated only with the  
 798 A-SAM. These correlations are consistent with the regression maps of geopo-  
 799 tential height in Figure 4 and their comparison with those obtained for SAM,  
 800 A-SAM and S-SAM by Campitelli et al (2022b).

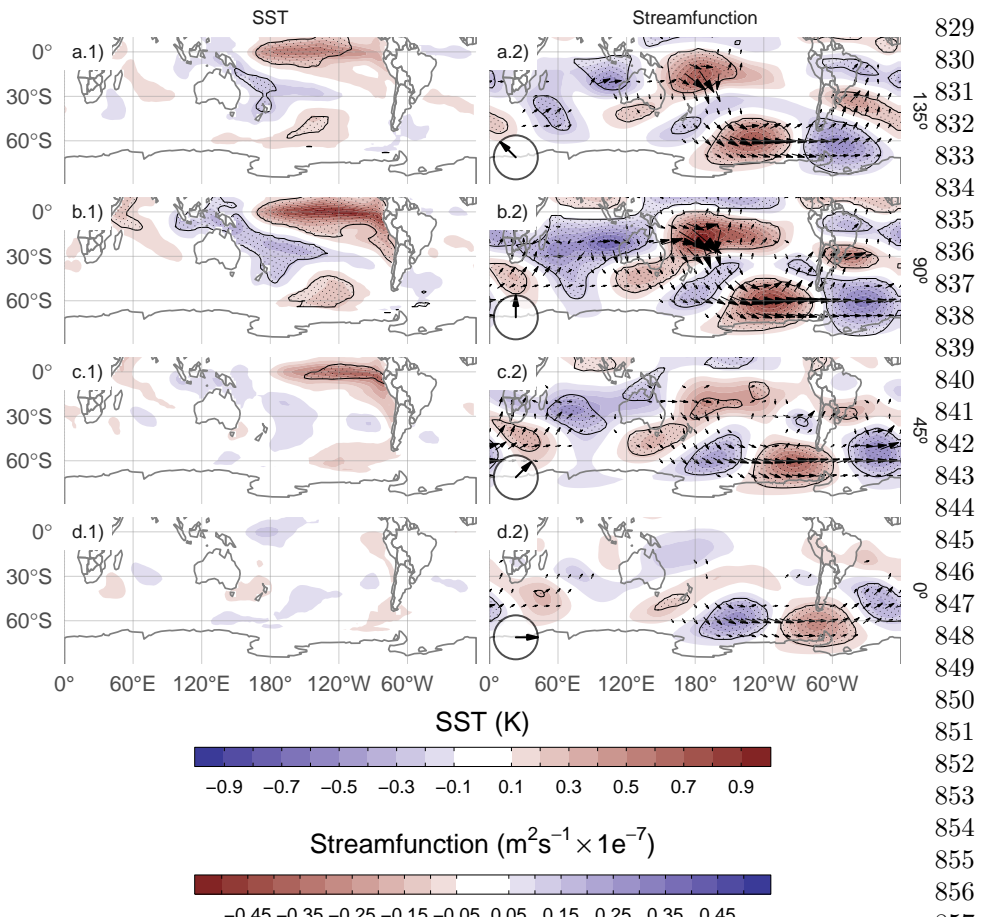
801 In the case of 90° cEOF2, its correlation with the SAM for the troposphere  
 802 is associated with the asymmetric variability of the SAM. Indeed, the 90°  
 803 cEOF2 shares up to 92% variance with the A-SAM and only 12% at most with  
 804 the S-SAM (Figure 10.b2). Such extremely high correlation between A-SAM  
 805 and 90° cEOF2 suggests that the modes obtained in this work are able to char-  
 806 acterise the zonally asymmetric component of the SAM described previously  
 807 by Campitelli et al (2022b).

808 **3.5 Tropical sources of cEOFs variabitliy**<sup>tropical</sup>

809 The connections between cEOFs and tropical sources of variability were also  
 810 assessed. Figure 11 shows the regression maps of Sea Surface Temperature  
 811 (SST) and streamfunction anomalies at 200 hPa upon standardised cEOF2.  
 812 As well as regression maps for the 0° and 90° phases, we include corresponding  
 813 regressions for two intermediate directions (corresponding to 45° and 135°).

814 The 90° cEOF2 (second row) is associated with strong positive SST anom-  
 815 alies on the Central to Eastern Pacific and negative anomalies over an area  
 816 across northern Australia, New Zealand the South Pacific Convergence Zone  
 817 (SPCZ) (Figure 11.b1). The regression field of SST anomalies bears a strong  
 818 resemblance with canonically positive ENSO (Bamston et al, 1997). Indeed,  
 819 there is a significant and very high correlation (0.76 (CI: 0.6 – 0.87)) between  
 820 the ONI and the 90° cEOF2 time series. In addition to the Pacific ENSO-like  
 821 pattern, there are also positive anomalies in the western Indian Ocean and  
 822 negative values in the eastern Indian Ocean, resembling a positive IOD (Saji  
 823 et al, 1999). Consistently, the correlation between the 90° cEOF2 and the DMI  
 824 is 0.62 (CI: 0.38 – 0.78).

825  
826  
827  
828



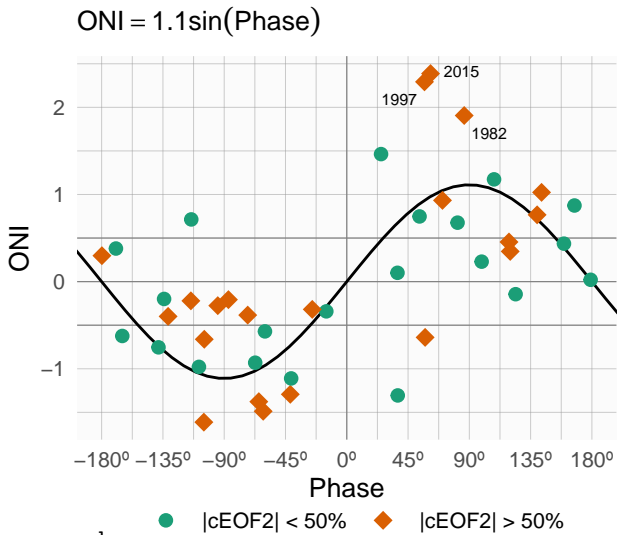
**Fig. 11:** Regression of SST (K, left column) and streamfunction zonal anomalies ( $m^2/s \times 10^{-7}$ , shaded) with their corresponding activity wave flux (vectors) (right column) upon cEOF2 different phases (illustrated in the lower-left arrow) for the 1979 – 2019 period. Areas marked with dots have p-values smaller than 0.01 adjusted for FDR.

fig:sst-psi-2

The  $90^\circ$  cEOF2 is associated with strong wave-like streamfunction anomalies emanating from the tropics (Figure 11.b2), both from the Central Pacific sector and the Indian Ocean. The atmospheric response associated with  $90^\circ$  cEOF2 is then consistent with the combined effect of ENSO and the IOD on the extratropics: with SST anomalies inducing anomalous tropical convection that in turn excite Rossby waves propagating meridionally towards higher latitudes (Mo, 2000; Cai et al., 2011a; Nuncio and Yuan, 2015).

However, the cEOF2 is not associated with the same tropical SST anomaly patterns at all their phases Figure 11.d1 and d2 show that the  $0^\circ$  cEOF2 is not associated either with any significant SST nor streamfunction anomalies

829  
830  
831  
832  
833  
834  
835  
836  
837  
838  
839  
840  
841  
842  
843  
844  
845  
846  
847  
848  
849  
850  
851  
852  
853  
854  
855  
856  
857  
858  
859  
860  
861  
862  
863  
864  
865  
866  
867  
868  
869  
870  
871  
872  
873  
874



**Fig. 12:** SON ONI values plotted against cEOF2 phase for the 1979 – 2019 period. Years with magnitude of cEOF2 greater (smaller) than the 50th percentile are shown as orange diamonds (green circles). Black line is the fit  $\text{ONI} \sim \sin(\text{phase})$  computed by weighted OLS using the magnitude of the cEOF2 as weights.

898 in the tropics. As a result, the correlation between the  $0^\circ$  cEOF2 and ENSO  
899 is not significant (0 (CI:  $-0.3 - 0.3$ )). Meanwhile, Rows a and c in Fig. 11 show  
900 that the intermediate phases are still associated with significant SST regressed  
901 anomalies over the Pacific Ocean, but at slightly different locations. The  $135^\circ$   
902 phase is associated with SST anomalies in the central Pacific (Fig. 11a.1),  
903 while the  $45^\circ$  phase is associated with SST anomalies in the eastern Pacific,  
904 which correspond roughly to the Central Pacific and Eastern Pacific “flavours”  
905 of ENSO, respectively (Fig. 11c.1) (Kao and Yu, 2009). Both phases are also  
906 associated with wave trains generated in the region surrounding Australia  
907 and propagates toward the extra-tropics, although less intense than the ones  
908 associated with the  $90^\circ$  phase.  
909

910 To further explore the relationship between tropical forcing and phases of  
911 the cEOF2, Figure 12 shows the ONI plotted against the cEOF2 phase for  
912 each SON trimester between 1979 and 2019, highlighting years in which the  
913 magnitude of cEOF2 is above the median. In years with positive (negative)  
914 ONI, the cEOF2 phase is mostly around  $90^\circ$  ( $-90^\circ$ ). In the neutral ENSO  
915 seasons, the cEOF2 phase is much more variable. The black line in Figure 12  
916 is a sinusoidal fit of the relationship between ONI and cEOF2 phase. The  $r^2$   
917 corresponding to the fit is 0.57, statistically significant with p-value  $< 0.001$ ,  
918 indicating a quasi-sinusoidal relation between these two variables.

919 The correlation between the absolute magnitude of the ONI and the cEOF2  
920 amplitude is 0.45 (CI: 0.17 – 0.66). However, this relationship is mostly

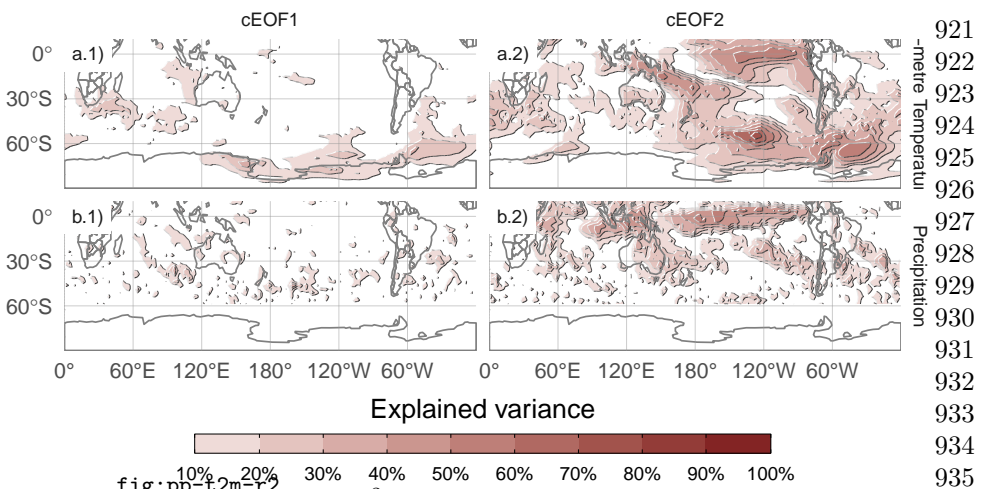


**Fig. 13:** Explained variance ( $r^2$  as percentage) of 2-metre temperature (row a) and precipitation (row b) anomalies by the regression upon cEOF1 (column 1) and cEOF2 (column 2).

driven by the three years with strongest ENSO events in the period (2015, 1997, and 1982) which coincide with the three years with strongest cEOF2 magnitude (not shown). If those years are removed, the correlation becomes non-significant (0.04 (CI: -0.28 – 0.35)). Furthermore, even when using all years, the Spearman correlation –which is robust to outliers– is also non-significant (0.2, p-value = 0.21). Therefore, although the location of tropical SST anomalies seem to have an effect in defining the phase of the cEOF2, the relationship between the magnitude of cEOF2 and ONI remains uncertain and might be only evident in very strong ENSO events, that are scarce in the historical observational record.

We conclude that the wave train represented by cEOF2 can be both part of the internal variability of the extratropical atmosphere and forced by tropical SSTs. In the former case, the wave train has little phase preference. However, when cEOF2 is excited by tropical SST variability, it tends to remain locked to the  $90^\circ$  phase. This explains the relative over-abundance of years with cEOF2 near positive and negative  $90^\circ$  phase in Figure 9.

Unlike the cEOF2 case, there are no significant SST regressed anomalies associated with either the  $0^\circ$  or  $90^\circ$  cEOF1 (Sup. Figure A.1). Consistently, streamfunction anomalies do not show any tropical influence. Instead, the  $0^\circ$  and  $90^\circ$  cEOF1 are associated with zonally propagating wave activity fluxes in the extra-tropics around  $60^\circ\text{S}$ , except for an equatorward flow from the coast of Antarctica around  $150^\circ\text{E}$  in the  $0^\circ$  phase. This suggests that the variability of cEOF1 is driven primary by the internal variability of the extra-tropics.

921  
922  
923  
924  
925  
926  
927  
928  
929  
930  
931  
932  
933  
934  
935  
936  
937  
938  
939  
940  
941  
942  
943  
944  
945  
946  
947  
948  
949  
950  
951  
952  
953  
954  
955  
956  
957  
958  
959  
960  
961  
962  
963  
964  
965  
966

967 **3.6 cEOFs surface impacts**

968 The influence of cEOFs variability in the anomalies of both 2-metre air tem-  
 969 perature and precipitation in the SH was also explored. Figure 13 shows the  
 970 2-meter temperature and precipitation anomalies explained variance by the  
 971 multiple linear model of both 0° and 90° cEOF1 (column 1), and both 0° and  
 972 90° cEOF2 (column 2). The variance explained by cEOF1 for precipitation  
 973 anomalies and temperature anomalies in most regions is extremely low, except  
 974 for the northern tip of the Antarctic Peninsula, northern Weddell Sea and the  
 975 Ross Sea coast (Fig. 13a.1).

976 This lack of strong relationship between the cEOF1 and SST, temperature  
 977 and precipitation might be surprising considering the correlation between the  
 978 cEOF1 and the SAM (Fig. 10 column 1) and the correlation between SAM and  
 979 Central Pacific SST, temperature east and west of the Antarctic Peninsula,  
 980 and with precipitation in western Australia (Fogt and Marshall, 2020). There  
 981 are two main reasons for this. First, the correlation between cEOF1 and the  
 982 SAM in the troposphere is modest, with less than 50% of shared variance (Fig.  
 983 10 column 1), so these indices are not expected to be equivalent to each other.  
 984 Second, Campitelli et al (2022b) showed that the strong relationship between  
 985 the SAM and Pacific SSTs and temperature anomalies around the Antarctic  
 986 Peninsula is mainly due to the asymmetric part of the SAM. Meanwhile, the  
 987 cEOF1 is significantly correlated only with the symmetric part of the SAM  
 988 (Fig. 10 column 1), which by itself is not significantly correlated with surface  
 989 temperatures in that area.

990 On the other hand, the cEOF2 explained variance is greater than 50% in  
 991 some regions for both variables (Fig. 13 column 2). For 2-metre temperature,  
 992 there are high values in the tropical Pacific and the SPCZ, as well as the  
 993 region following an arc between New Zealand and the South Atlantic, with  
 994 higher values in the Southern Ocean. Over the continents, there are moderate  
 995 values of about 30% variance explained in southern Australia, Southern South  
 996 America and the Antarctic Peninsula. For precipitation, there are high values  
 997 over the tropics. At higher latitudes, moderate values are observed over eastern  
 998 Australia and some regions of southern South America.

999 Since the cEOF1 has a relatively weak signal in the surface variables  
 1000 explored here, we will only focus on the cEOF2 influence. Figure 14 shows  
 1001 regression maps of 2-metre temperature (column 1) and precipitation (column  
 1002 2) anomalies upon different phases of standardised cEOF2.

1003 Temperature anomalies associated with the 90° cEOF (Fig. 14.b1) show  
 1004 positive values in the tropical Pacific, consistent with SSTs anomalies associ-  
 1005 ated with the same phase (Fig. 11.b1). At higher latitudes there is a wave-like  
 1006 pattern of positive and negative values that coincide with the nodes of the  
 1007 850 hPa geopotential height regression patterns. This is consistent with tem-  
 1008 perature anomalies produced by meridional advection of temperature by the  
 1009 meridional winds arising from geostrophic balance. Over the continents, the  
 1010 90° cEOF2 (Fig. 14b.1) is associated with positive regressed temperature  
 1011

1012

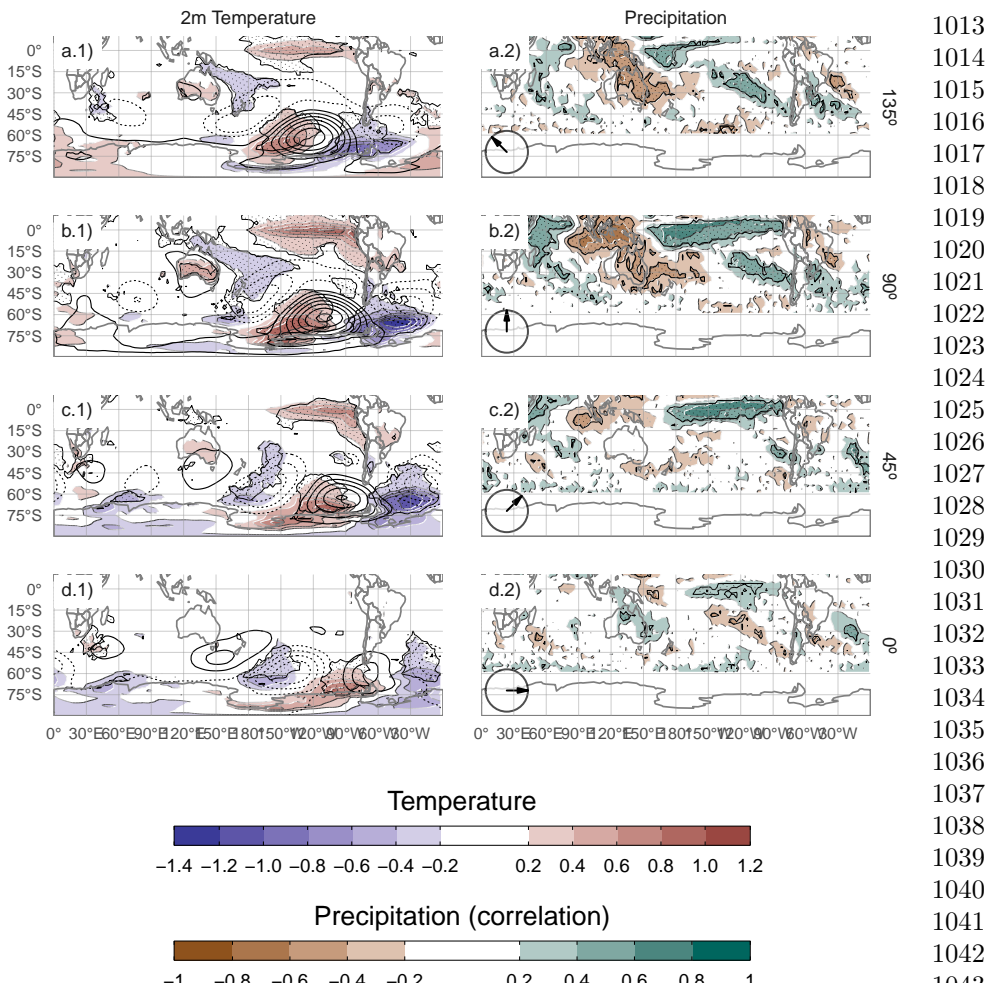


**Fig. 14:** `fig:pp-temp-2` Regression of SON mean 2-meter temperature (K, shaded) and 850 hPa geopotential height (m, contours) (column 1), and precipitation (correlation, column 2) upon different phases of cEOF2. For the 1979 – 2019. Areas marked with dots have p-values smaller than 0.01 adjusted for False Detection Rate.

anomalies in southern Australia and negative regressed anomalies in southern South America and the Antarctic Peninsula, that are a result of the wave train described before.

The temperatures anomalies associated with the  $0^\circ$  cEOF2 (Fig. 14d.1) are less extensive and restricted to mid and high latitudes.

Over the continents, the temperature anomalies regressions are non significant, except for positive anomalies near the Antarctic Peninsula.

24 *SH zonally asymmetric circulation with cEOF*

1059 Tropical precipitation anomalies associated with the 90° cEOF2 are strong,  
 1060 with positive anomalies in the central Pacific and western Indian, and negative  
 1061 anomalies in the eastern Pacific (Fig. 14b.2). This field is consistent with  
 1062 the SST regression map (Fig. 14b.1) as the positive SST anomalies enhance  
 1063 tropical convection and the negative SST anomalies inhibits it.

1064 In the extra-tropics, the positive 90° cEOF2 is related to drier conditions  
 1065 over eastern Australia and the surrounding ocean, that it is similar signal as  
 1066 the one associated with ENSO (Cai et al, 2011a). However, the 90° cEOF2  
 1067 is not the phase most correlated with precipitation in that area. The 135°  
 1068 phase (an intermediate between positive 90° and 180° cEOF2) component  
 1069 is associated with stronger and more extensive temporal correlations with  
 1070 precipitation over Australia and New Zealand, consistent with the effect of  
 1071 ENSO on precipitation in that region. These anomalies are probably related  
 1072 to the direct effect of vertical anomalies of the Southern Oscillation and less  
 1073 so to the large-scale circulation anomalies described by cEOF2 (Cai et al,  
 1074 2011b). Circulation anomalies associated with the Indian Ocean Dipole could  
 1075 also play a role (Cai et al, 2011b).

1076 Over South America, the 90° cEOF2 has positive correlations with precipi-  
 1077 tation in South Eastern South America (SESA) and central Chile, and negative  
 1078 correlations in eastern Brazil. This correlation field matches the springtime  
 1079 precipitation signature of ENSO (e.g. Cai et al, 2020) and it is also similar  
 1080 to the precipitation anomalies associated with the A-SAM (Campitelli et al,  
 1081 2022b). This result is not surprising considering the close relationship of the  
 1082 90° cEOF2 with both ONI and A-SAM index, which was shown previously.  
 1083 Furthermore, it consolidates the identification of the cEOF2 with the PSA  
 1084 pattern. Resembling the relationship between ONI and the phase of cEOF2  
 1085 (Fig. 12), there is a cEOF2 phase dependence of the precipitation anomalies  
 1086 in SESA (not shown).

1087 The correlation coefficients between precipitation anomalies and the 0°  
 1088 cEOF2 (Fig. 14d.2) are weaker than for 90° cEOF2. There is a residual pos-  
 1089 itive correlation in the equatorial eastern Pacific and small, not statistically  
 1090 significant positive correlations over eastern Australia and negative ones over  
 1091 New Zealand.

1092

## 1093 4 Discussion and conclusions

1094 discussion  
 1095 In this study we assessed extratropical Southern Hemisphere zonally asym-  
 1096 metric circulation in austral spring. For this purpose, we derived two complex  
 1097 indices using Complex Empirical Orthogonal Functions and used to charac-  
 1098 terise both amplitude and phase of planetary waves.

1099 The cEOF1 represents the variability of the zonal wave 1 in the strato-  
 1100 sphere and is closely related to stratospheric variability such as anomalies in  
 1101 Total Column Ozone. Otherwise, this complex EOF is not related with SST  
 1102 variability and continental precipitation in the Southern Hemisphere. On the  
 1103 other hand, the cEOF2 represents a wave-3 pattern with maximum magnitude  
 1104

in the Pacific sector, that is an alternative representation of the PSA1 and PSA2 patterns (Mo and Paegle 2001). The 90° cEOF2 can be identified with the PSA1 and the 0° cEOF2 with the PSA2. While the cEOF2 variability is related to surface impacts, the cEOF1 surface influence is almost negligible. For instance, precipitation anomalies in South America associated with the 90° cEOF2 show a clear ENSO-like impact, with positive anomalies in South-eastern South America, negative anomalies in Southern Brazil and positive anomalies in central Chile for positive 90° cEOF2 phase.

Variability patterns that arise from cEOF methodology describe the zonally asymmetric springtime extratropical SH circulation, reproducing previous features such as the variability related to PSAs or A-SAM.

Since the spatial fields obtained from both components of cEOF2, which resemble PSA patterns, are in quadrature by construction, the cEOF methodology allows to derive, for the first time to our knowledge, a joint PSA index from the resulted amplitude and phase. These patterns are not forced to be orthogonal to other modes of circulation, like they are in standard EOF methodology. This allows us to show for example, that the 90° cEOF2, corresponding to PSA1 variability, is closely associated with the SAM in the troposphere. Previous research in the SAM–PSA relationship had the issue that the SAM and the PSA patterns are not independently derived and so the correlation between these indices had to be zero by construction (e.g. Yu et al. 2015).

Most studies on the relationship between ENSO and SAM rely on correlations between an ENSO index and the SAM index (e.g. L'Heureux and Thompson, 2006, Cai et al (2011c)) or between the SAM index and other variables associated with tropical convection, such as OLR or tropical SSTS (e.g. Carvalho et al, 2005). However, Campitelli et al (2022b) showed that the correlation between ENSO and SAM is almost completely explained by the asymmetric component of the SAM. In this work we show that the asymmetric component of the SAM can be identified with the PSA1. Therefore, the correlation between ENSO and SAM in SON is predominantly the correlation between ENSO and PSA1, at least in SON. This sheds new light into the previous literature, as it cannot be assumed that a high correlation between ENSO and SAM indexes indicates a relationship between ENSO and zonally symmetric variability.

Further investigation is necessary to determine the connection between the symmetric component of the SAM and the PSA. It is possible that the PSA may force a zonally symmetric response (or vice versa) via wave-zonal mean flow interactions (Kim and Lee, 2004), or that this correlation is simply a statistical artefact resulting from the EOF methodology used to define the SAM and the fact that the spatial structure of the PSA projects onto the spatial structure of the symmetric SAM.

Irving and Simmonds (2016) argued that there is some disagreement in the literature of whether the phase of the PSA pattern is affected by the location of tropical SST anomalies. With the methodology used in this study, we were

26 *SH zonally asymmetric circulation with cEOF*

1151 able to show not only that the cEOF2 tends to be in the positive or negative  
 1152 90° phase (~PSA1) when the ENSO region is warm or cold, respectively, but  
 1153 also that central Pacific SST anomalies tend to align the cEOF towards the  
 1154 negative 0° phase and eastern Pacific SST anomalies tend to align it towards  
 1155 positive 0° phase. When ENSO phase is neutral, the cEOF2 is still as active,  
 1156 but with no preferred phase. The latter agrees with the results of Cai and  
 1157 Watterson (2002), who showed that the CSIRO Model can develop PSA-like  
 1158 variability even in the absence of ENSO forcing (i.e. with a climatological  
 1159 run), but that the variability of one of the PSA modes was enhanced when  
 1160 adding the ENSO signal. The sensitivity of the phase of the PSAs to the  
 1161 location of the tropical SST anomalies was also seen by Ciasto et al (2015),  
 1162 who detected similar Rossby wave patterns associated with central Pacific and  
 1163 eastern Pacific SST anomalies but with a change in phase.

1164 The method used in this study has similarities to the one used by Goyal  
 1165 et al (2022) as they construct an index of amplitude and phase of zonal  
 1166 wave 3-like variability by combining the two leading EOFs of meridional wind  
 1167 anomalies. The patterns obtained by them bear high resemblance with cEOF2.  
 1168 Although a detailed comparison is out of scope for this paper, the cEOF anal-  
 1169 ysis has the advantage of constructing the indices based on patterns that are  
 1170 exactly in quadrature by construction.

1171 The methodology proposed in this study allows for a deeper understanding  
 1172 of the zonally asymmetric springtime extratropical SH circulation such as a  
 1173 better description of PSA like variability using a unique complex index and the  
 1174 understanding of relationship between PSAs and ENSO or SAM variability.  
 1175 Further work should extend this analysis to other seasons and further study  
 1176 the relationship between the cEOF2 and the SAM.

1177

## 1178 **Declarations**

1179 declarations

## 1180 **Funding**

1181 The research was supported by UBACyT20020170100428BA, Consejo  
 1182 Nacional de Investigaciones Científicas y Técnicas (CONICET) PIP  
 1183 11220200102038CO, PICT-2020-SERIEA-I-INVI-00540, and the CLIMAX  
 1184 Project funded by Belmont Forum/ANR-15-JCL/-0002-01. Elio Campitelli  
 1185 was supported by a PhD grant from CONICET, Argentina.  
 1186

1187

## 1188 **Conflict of interest/Competing interests**

1189 conflict-of-interestcompeting-interests

1190 The authors have no relevant financial or non-financial interests to disclose.

1191

## 1192 **Ethics approval**

1193 ethics-approval

1194 Not applicable.

1195

1196

<b>Consent to participate</b>	consent-to-participate	1197
Not applicable.		1198
		1199
<b>Consent for publication</b>	consent-for-publication	1200
Not applicable.		1201
		1202
		1203
<b>Availability of data and materials</b>	availability-of-data-and-materials	1204
All data used in this paper available in a Zenodo repository (Campitelli et al, 2022a) ( <a href="https://zenodo.org/record/6612429">https://zenodo.org/record/6612429</a> ). Indices updated monthly and daily will be made available at <a href="http://www.cima.fcen.uba.ar/~elio.campitelli/shceof/">http://www.cima.fcen.uba.ar/~elio.campitelli/shceof/</a> .		1205
		1206
		1207
		1208
		1209
		1210
		1211
		1212
		1213
		1214
		1215
		1216
		1217
		1218
		1219
		1220
		1221
		1222
		1223
		1224
		1225
		1226
		1227
		1228
		1229
		1230
<b>Code availability</b>	code-availability	1231
A version-controlled repository of the code used to create this analysis, including the code used to download the data can be found at <a href="https://github.com/eliocamp/shceof">https://github.com/eliocamp/shceof</a> .		1232
		1233
		1234
		1235
<b>Authors' contributions</b>	authors-contributions	1236
E.C. made the data curation, formal analysis and prepared all the figures.		1237
E.C. and L.D. wrote the main manuscript text. All authors reviewed the manuscript.		1238
		1239
		1240
		1241
		1242

**1243 A Extra figures**

1244

**extra-figures**

1245

1246

1247

1248

1249

1250

1251

1252

1253

1254

1255

1256

1257

1258

1259

1260

1261

1262

1263

1264

1265

1266

1267

1268

1269

1270

1271

1272

1273

1274

1275

1276

1277

1278

1279

1280

1281

1282

1283

1284

1285

1286

1287

1288

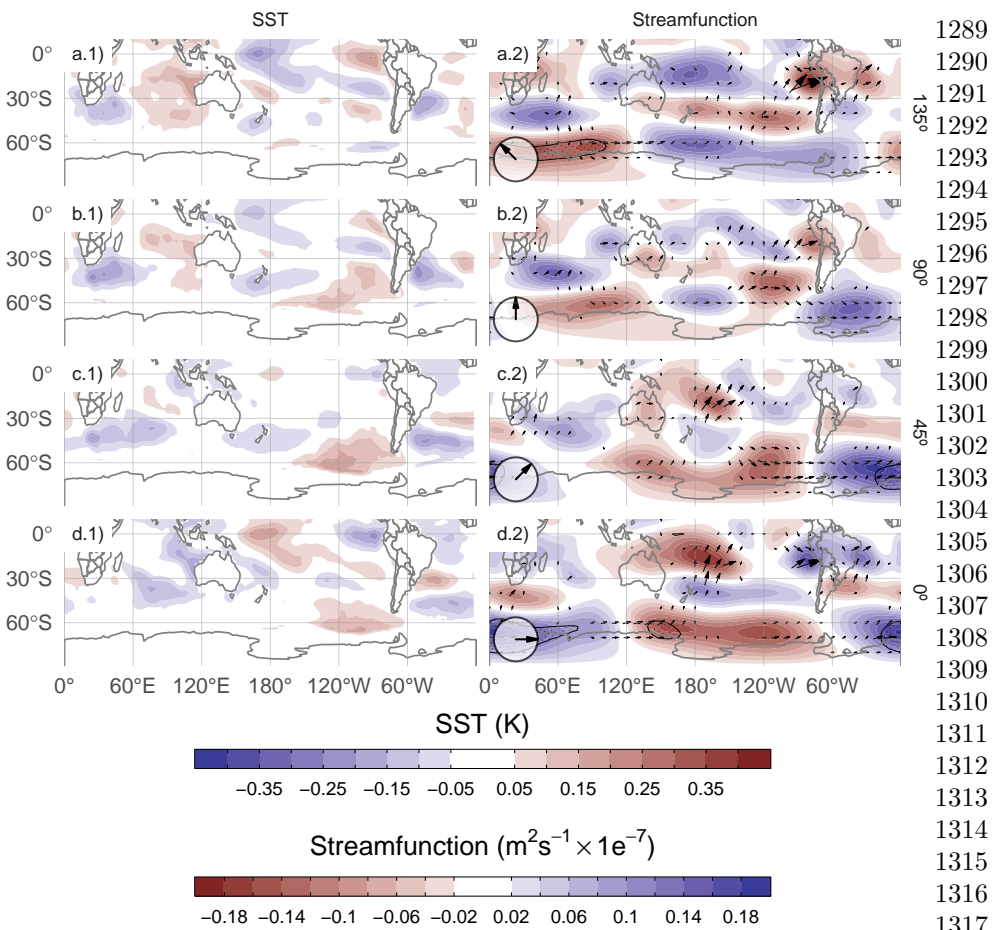


**Fig. A.1:** Same as Figure 11 but for cEOF1.

fig:sst-psi-1

## References

- Adams JC, Swartztrauber PN, Sweet R (1999) FISHPACK, a package of Fortran subprograms for the solution of separable elliptic partial differential equations. <https://www2.cisl.ucar.edu/resources/legacy/fishpack>
- Albers S, Campitelli E (2020) Rsoi: Import Various Northern and Southern Hemisphere Climate Indices
- Allaire JJ, Xie [aut Y, cre, et al (2020) Rmarkdown: Dynamic Documents for R
- Baldwin MP, Thompson DWJ (2009) A critical comparison of stratosphere–troposphere coupling indices. Quarterly Journal of the Royal Meteorological Society 135(644):1661–1672. <https://doi.org/10.1002/qj.479>

1289  
1290  
1291  
1292  
1293  
1294  
1295  
1296  
1297  
1298  
1299  
1300  
1301  
1302  
1303  
1304  
1305  
1306  
1307  
1308  
1309  
1310  
1311  
1312  
1313  
1314  
1315  
1316  
1317  
1318  
1319  
1320  
1321  
1322  
1323  
1324  
1325  
1326  
1327  
1328  
1329  
1330  
1331  
1332  
1333  
1334

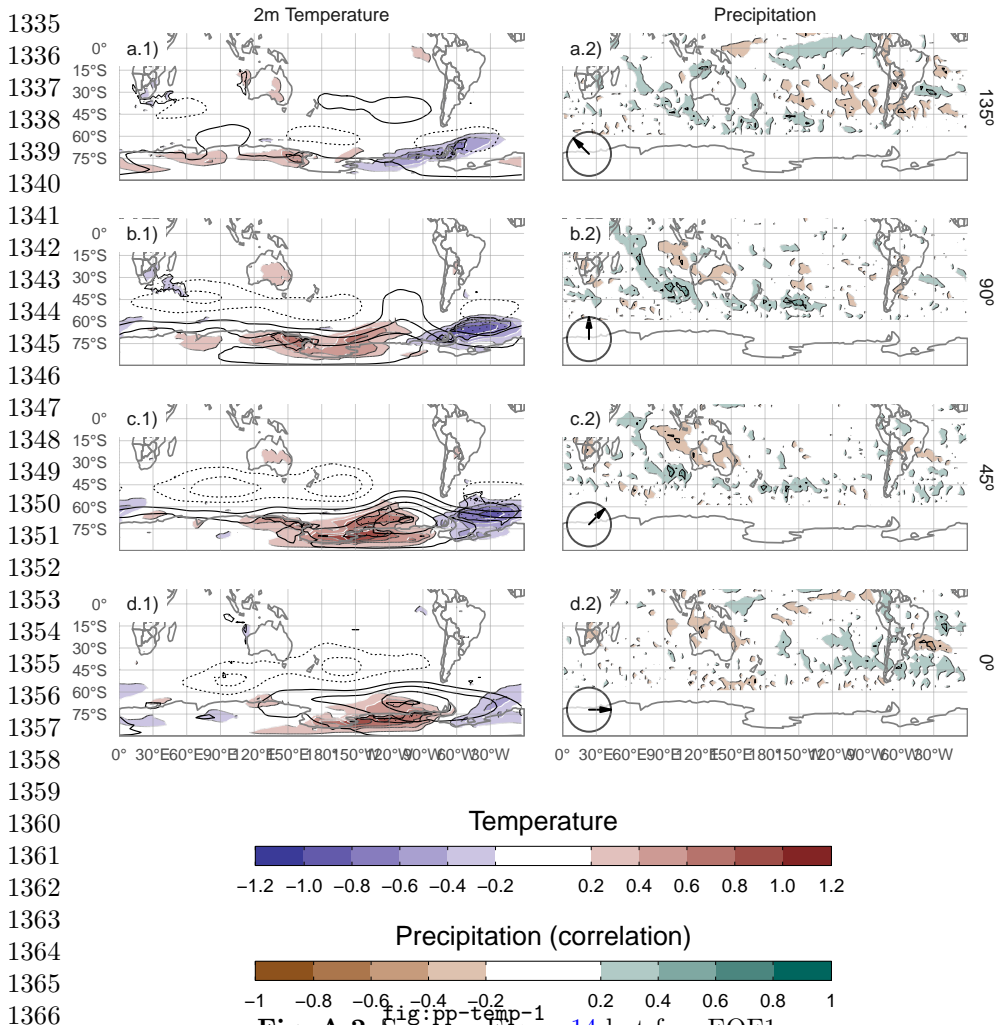
30 *SH zonally asymmetric circulation with cEOF*

Fig. A.2: Same as Figure 14 but for cEOF1.

- 1369 Bamston AG, Chelliah M, Goldenberg SB (1997) Documentation of a  
 1370 highly ENSO-related sst region in the equatorial pacific: Research note.  
 1371 *Atmosphere-Ocean* 35(3):367–383. <https://doi.org/10.1080/07055900.1997.9649597>  
 1373
- 1374 Bell B, Hersbach H, Berrisford P, et al (2020) ERA5 monthly  
 1375 averaged data on pressure levels from 1950 to 1978 (pre-  
 1376 liminary version). Copernicus Climate Change Service (C3S)  
 1377 Climate Data Store (CDS) (Accessed on <26-08-2021>),  
 1378 [https://cds.climate.copernicus.eu/cdsapp#!/dataset/reanalysis-era5-](https://cds.climate.copernicus.eu/cdsapp#!/dataset/reanalysis-era5-pressure-levels-monthly-means-preliminary-back-extension?tab=overview)  
 1379 [pressure-levels-monthly-means-preliminary-back-extension?tab=overview](https://cds.climate.copernicus.eu/cdsapp#!/dataset/reanalysis-era5-pressure-levels-monthly-means-preliminary-back-extension?tab=overview)  
 1380

- Benjamini Y, Hochberg Y (1995) Controlling the False Discovery Rate: A Practical and Powerful Approach to Multiple Testing. *Journal of the Royal Statistical Society: Series B (Methodological)* 57(1):289–300. <https://doi.org/10.1111/j.2517-6161.1995.tb02031.x> 1381  
1382  
1383  
1384  
1385  
1386  
1387  
1388  
1389  
1390  
1391  
1392  
1393  
1394  
1395  
1396  
1397  
1398  
1399  
1400  
1401  
1402  
1403  
1404  
1405  
1406  
1407  
1408  
1409  
1410  
1411  
1412  
1413  
1414  
1415  
1416  
1417  
1418  
1419  
1420  
1421  
1422  
1423  
1424  
1425  
1426
- Cai W, Watterson IG (2002) Modes of Interannual Variability of the Southern Hemisphere Circulation Simulated by the CSIRO Climate Model. *Journal of Climate* 15(10):1159–1174. [https://doi.org/10.1175/1520-0442\(2002\)015<1159:MOIVOT>2.0.CO;2](https://doi.org/10.1175/1520-0442(2002)015<1159:MOIVOT>2.0.CO;2) 1381  
1382  
1383  
1384  
1385  
1386  
1387  
1388  
1389  
1390  
1391  
1392  
1393  
1394  
1395  
1396  
1397  
1398  
1399  
1400  
1401  
1402  
1403  
1404  
1405  
1406  
1407  
1408  
1409  
1410  
1411  
1412  
1413  
1414  
1415  
1416  
1417  
1418  
1419  
1420  
1421  
1422  
1423  
1424  
1425  
1426
- Cai W, van Renssch P, Cowan T, et al (2011a) Teleconnection Pathways of ENSO and the IOD and the Mechanisms for Impacts on Australian Rainfall. *Journal of Climate* 24(15):3910–3923. <https://doi.org/10.1175/2011JCLI4129.1> 1381  
1382  
1383  
1384  
1385  
1386  
1387  
1388  
1389  
1390  
1391  
1392  
1393  
1394  
1395  
1396  
1397  
1398  
1399  
1400  
1401  
1402  
1403  
1404  
1405  
1406  
1407  
1408  
1409  
1410  
1411  
1412  
1413  
1414  
1415  
1416  
1417  
1418  
1419  
1420  
1421  
1422  
1423  
1424  
1425  
1426
- Cai W, van Renssch P, Cowan T, et al (2011b) Teleconnection Pathways of ENSO and the IOD and the Mechanisms for Impacts on Australian Rainfall. *Journal of Climate* 24(15):3910–3923. <https://doi.org/10.1175/2011JCLI4129.1> 1381  
1382  
1383  
1384  
1385  
1386  
1387  
1388  
1389  
1390  
1391  
1392  
1393  
1394  
1395  
1396  
1397  
1398  
1399  
1400  
1401  
1402  
1403  
1404  
1405  
1406  
1407  
1408  
1409  
1410  
1411  
1412  
1413  
1414  
1415  
1416  
1417  
1418  
1419  
1420  
1421  
1422  
1423  
1424  
1425  
1426
- Cai W, Sullivan A, Cowan T (2011c) Interactions of ENSO, the IOD, and the SAM in CMIP3 Models. *Journal of Climate* 24(6):1688–1704. <https://doi.org/10.1175/2010JCLI3744.1> 1381  
1382  
1383  
1384  
1385  
1386  
1387  
1388  
1389  
1390  
1391  
1392  
1393  
1394  
1395  
1396  
1397  
1398  
1399  
1400  
1401  
1402  
1403  
1404  
1405  
1406  
1407  
1408  
1409  
1410  
1411  
1412  
1413  
1414  
1415  
1416  
1417  
1418  
1419  
1420  
1421  
1422  
1423  
1424  
1425  
1426
- Cai W, McPhaden MJ, Grimm AM, et al (2020) Climate impacts of the El Niño–Southern Oscillation on South America. *Nature Reviews Earth & Environment* 1(4):215–231. <https://doi.org/10.1038/s43017-020-0040-3> 1381  
1382  
1383  
1384  
1385  
1386  
1387  
1388  
1389  
1390  
1391  
1392  
1393  
1394  
1395  
1396  
1397  
1398  
1399  
1400  
1401  
1402  
1403  
1404  
1405  
1406  
1407  
1408  
1409  
1410  
1411  
1412  
1413  
1414  
1415  
1416  
1417  
1418  
1419  
1420  
1421  
1422  
1423  
1424  
1425  
1426
- Campitelli E (2020) metR: Tools for Easier Analysis of Meteorological Fields 1381  
1382  
1383  
1384  
1385  
1386  
1387  
1388  
1389  
1390  
1391  
1392  
1393  
1394  
1395  
1396  
1397  
1398  
1399  
1400  
1401  
1402  
1403  
1404  
1405  
1406  
1407  
1408  
1409  
1410  
1411  
1412  
1413  
1414  
1415  
1416  
1417  
1418  
1419  
1420  
1421  
1422  
1423  
1424  
1425  
1426
- Campitelli E, Díaz L, Vera C (2022a) Data for "Revisiting the Austral Spring Extratropical Southern Hemisphere zonally asymmetric circulation using complex Empirical Orthogonal Functions". <https://doi.org/10.5281/zenodo.6612324> 1381  
1382  
1383  
1384  
1385  
1386  
1387  
1388  
1389  
1390  
1391  
1392  
1393  
1394  
1395  
1396  
1397  
1398  
1399  
1400  
1401  
1402  
1403  
1404  
1405  
1406  
1407  
1408  
1409  
1410  
1411  
1412  
1413  
1414  
1415  
1416  
1417  
1418  
1419  
1420  
1421  
1422  
1423  
1424  
1425  
1426
- Campitelli E, Díaz LB, Vera C (2022b) Assessment of zonally symmetric and asymmetric components of the Southern Annular Mode using a novel approach. *Climate Dynamics* 58(1):161–178. <https://doi.org/10.1007/s00382-021-05896-5> 1381  
1382  
1383  
1384  
1385  
1386  
1387  
1388  
1389  
1390  
1391  
1392  
1393  
1394  
1395  
1396  
1397  
1398  
1399  
1400  
1401  
1402  
1403  
1404  
1405  
1406  
1407  
1408  
1409  
1410  
1411  
1412  
1413  
1414  
1415  
1416  
1417  
1418  
1419  
1420  
1421  
1422  
1423  
1424  
1425  
1426
- Carvalho LMV, Jones C, Ambrizzi T (2005) Opposite Phases of the Antarctic Oscillation and Relationships with Intraseasonal to Interannual Activity in the Tropics during the Austral Summer. *Journal of Climate* 18(5):702–718. <https://doi.org/10.1175/JCLI-3284.1> 1381  
1382  
1383  
1384  
1385  
1386  
1387  
1388  
1389  
1390  
1391  
1392  
1393  
1394  
1395  
1396  
1397  
1398  
1399  
1400  
1401  
1402  
1403  
1404  
1405  
1406  
1407  
1408  
1409  
1410  
1411  
1412  
1413  
1414  
1415  
1416  
1417  
1418  
1419  
1420  
1421  
1422  
1423  
1424  
1425  
1426

- 1427 Cazes-Boezio G, Robertson AW, Mechoso CR (2003) Seasonal Dependence of  
 1428 ENSO Teleconnections over South America and Relationships with Precipi-  
 1429 tation in Uruguay. *Journal of Climate* 16(8):1159–1176. [https://doi.org/10.1175/1520-0442\(2003\)16<1159:SDETO>2.0.CO;2](https://doi.org/10.1175/1520-0442(2003)16<1159:SDETO>2.0.CO;2)
- 1431
- 1432 Ciasto LM, Simpkins GR, England MH (2015) Teleconnections between Tropi-  
 1433 cal Pacific SST Anomalies and Extratropical Southern Hemisphere Climate.  
 1434 *Journal of Climate* 28(1):56–65. <https://doi.org/10.1175/JCLI-D-14-00438.1>
- 1435
- 1436 Dowle M, Srinivasan A (2020) Data.table: Extension of 'data.frame'  
 1437
- 1438 Fogt RL, Marshall GJ (2020) The Southern Annular Mode: Variability, trends,  
 1439 and climate impacts across the Southern Hemisphere. *WIREs Climate  
 1440 Change* 11(4):e652. <https://doi.org/10.1002/wcc.652>
- 1441
- 1442 Gelbrecht M, Boers N, Kurths J (2018) Phase coherence between precipita-  
 1443 tion in South America and Rossby waves. *Science Advances* 4(12):eaau3191.  
 1444 <https://doi.org/10.1126/sciadv.aau3191>
- 1445
- 1446 Gong D, Wang S (1999) Definition of Antarctic Oscillation index. *Geophysical  
 1447 Research Letters* 26(4):459–462. <https://doi.org/10.1029/1999GL900003>
- 1448
- 1449 Goyal R, Jucker M, Gupta AS, et al (2022) A new zonal wave 3 index for the  
 1450 Southern Hemisphere. *Journal of Climate* -1(aop):1–25
- 1451
- 1452 Grytsai A (2011) Planetary wave peculiarities in Antarctic ozone distribution  
 1453 during 1979–2008. *International Journal of Remote Sensing* 32(11):3139–  
 1454 3151. <https://doi.org/10.1080/01431161.2010.541518>
- 1455
- 1456 Hartmann DL, Garcia RR (1979) A Mechanistic Model of Ozone Trans-  
 1457 port by Planetary Waves in the Stratosphere. *Journal of the Atmo-  
 1458 spheric Sciences* 36(2):350–364. [https://doi.org/10.1175/1520-0469\(1979\)036<0350:AMMOOT>2.0.CO;2](https://doi.org/10.1175/1520-0469(1979)036<0350:AMMOOT>2.0.CO;2)
- 1459
- 1460 Hersbach H, Bell B, Berrisford P, et al (2019) ERA5 monthly averaged data  
 1461 on pressure levels from 1979 to present. Copernicus Climate Change Service  
 1462 (C3S) Climate Data Store (CDS) (Accessed on <13-03-2023>). <https://doi.org/10.24381/cds.6860a573>
- 1463
- 1464
- 1465 Hobbs WR, Raphael MN (2010) Characterizing the zonally asymmetric com-  
 1466 ponent of the SH circulation. *Climate Dynamics* 35(5):859–873. <https://doi.org/10.1007/s00382-009-0663-z>
- 1467
- 1468
- 1469 Horel JD (1984) Complex Principal Component Analysis: Theory and Exam-  
 1470 ples. *Journal of Applied Meteorology and Climatology* 23(12):1660–1673.  
 1471 [https://doi.org/10.1175/1520-0450\(1984\)023<1660:CPCATA>2.0.CO;2](https://doi.org/10.1175/1520-0450(1984)023<1660:CPCATA>2.0.CO;2)
- 1472

- Hoskins BJ, Hodges KI (2005) A New Perspective on Southern Hemisphere Storm Tracks. *Journal of Climate* 18(20):4108–4129. <https://doi.org/10.1175/JCLI3570.1> 1473  
1474  
1475  
1476  
1477  
1478  
1479  
1480  
1481  
1482  
1483  
1484  
1485  
1486  
1487  
1488  
1489  
1490  
1491  
1492  
1493  
1494  
1495  
1496  
1497  
1498  
1499  
1500  
1501  
1502  
1503  
1504  
1505  
1506  
1507  
1508  
1509  
1510  
1511  
1512  
1513  
1514  
1515  
1516  
1517  
1518
- Huang B, Thorne PW, Banzon VF, et al (2017) Extended Reconstructed Sea Surface Temperature, Version 5 (ERSSTv5): Upgrades, Validations, and Intercomparisons. *Journal of Climate* 30(20):8179–8205. <https://doi.org/10.1175/JCLI-D-16-0836.1>
- Hufkens K (2020) Ecmwfr: Programmatic interface to the two European Centre for Medium-Range Weather Forecasts API services
- Irving D, Simmonds I (2015) A Novel Approach to Diagnosing Southern Hemisphere Planetary Wave Activity and Its Influence on Regional Climate Variability. *Journal of Climate* 28(23):9041–9057. <https://doi.org/10.1175/JCLI-D-15-0287.1>
- Irving D, Simmonds I (2016) A New Method for Identifying the Pacific–South American Pattern and Its Influence on Regional Climate Variability. *Journal of Climate* 29(17):6109–6125. <https://doi.org/10.1175/JCLI-D-15-0843.1>
- Kao HY, Yu JY (2009) Contrasting Eastern-Pacific and Central-Pacific Types of ENSO. *Journal of Climate* 22(3):615–632. <https://doi.org/10.1175/2008JCLI2309.1>
- Katz RW, Brown BG (1991) The problem of multiplicity in research on teleconnections. *International Journal of Climatology* 11(5):505–513. <https://doi.org/10.1002/joc.3370110504>
- Kim Hk, Lee S (2004) The Wave–Zonal Mean Flow Interaction in the Southern Hemisphere. *Journal of the Atmospheric Sciences* 61(9):1055–1067. [https://doi.org/10.1175/1520-0469\(2004\)061<1055:TWMFII>2.0.CO;2](https://doi.org/10.1175/1520-0469(2004)061<1055:TWMFII>2.0.CO;2)
- Krokhin VV, Luxemburg WMJ (2007) Temperatures and precipitation totals over the Russian Far East and Eastern Siberia: Long-term variability and its links to teleconnection indices. *Hydrology and Earth System Sciences* 11(6):1831–1841. <https://doi.org/10.5194/hess-11-1831-2007>
- L’Heureux ML, Thompson DWJ (2006) Observed Relationships between the El Niño–Southern Oscillation and the Extratropical Zonal-Mean Circulation. *Journal of Climate* 19(2):276–287. <https://doi.org/10.1175/JCLI3617.1>
- Lim EP, Hendon HH, Thompson DWJ (2018) Seasonal Evolution of Stratosphere-Troposphere Coupling in the Southern Hemisphere and Implications for the Predictability of Surface Climate. *Journal of Geophysical Research: Atmospheres* 123(21):12,002–12,016. <https://doi.org/10.1029/2017JD027501>

34 *SH zonally asymmetric circulation with cEOF*

- 1519 2018JD029321  
1520  
1521 Mo KC (2000) Relationships between Low-Frequency Variability in the  
1522 Southern Hemisphere and Sea Surface Temperature Anomalies. *Journal*  
1523 of Climate 13(20):3599–3610. [https://doi.org/10.1175/1520-0442\(2000\)013<3599:RBLFVI>2.0.CO;2](https://doi.org/10.1175/1520-0442(2000)013<3599:RBLFVI>2.0.CO;2)  
1524  
1525 Mo KC, Paegle JN (2001) The Pacific–South American modes and their  
1526 downstream effects. *International Journal of Climatology* 21(10):1211–1229.  
1527 <https://doi.org/10.1002/joc.685>  
1528  
1529 Nuncio M, Yuan X (2015) The Influence of the Indian Ocean Dipole on Antarc-  
1530 tic Sea Ice. *Journal of Climate* 28(7):2682–2690. <https://doi.org/10.1175/JCLI-D-14-00390.1>  
1531  
1532  
1533 Pezza AB, Rashid HA, Simmonds I (2012) Climate links and recent  
1534 extremes in antarctic sea ice, high-latitude cyclones, Southern Annular  
1535 Mode and ENSO. *Climate Dynamics* 38(1):57–73. <https://doi.org/10.1007/s00382-011-1044-y>  
1536  
1537  
1538 Plumb RA (1985) On the Three-Dimensional Propagation of Stationary  
1539 Waves. *Journal of the Atmospheric Sciences* 42(3):217–229. [https://doi.org/10.1175/1520-0469\(1985\)042<0217:OTTDPO>2.0.CO;2](https://doi.org/10.1175/1520-0469(1985)042<0217:OTTDPO>2.0.CO;2)  
1540  
1541 R Core Team (2020) R: A Language and Environment for Statistical Com-  
1542 puting. R Foundation for Statistical Computing, Vienna, Austria  
1543  
1544  
1545 Raphael M (2003) Recent, Large-Scale Changes in the Extratropical Southern  
1546 Hemisphere Atmospheric Circulation. *Journal of Climate* 16(17):2915–2924.  
1547 [https://doi.org/10.1175/1520-0442\(2003\)016<2915:RLCITE>2.0.CO;2](https://doi.org/10.1175/1520-0442(2003)016<2915:RLCITE>2.0.CO;2)  
1548  
1549 Raphael MN (2004) A zonal wave 3 index for the Southern Hemisphere. *Geo-*  
1550 *physical Research Letters* 31(23). <https://doi.org/10.1029/2004GL020365>  
1551  
1552 Raphael MN (2007) The influence of atmospheric zonal wave three on  
1553 Antarctic sea ice variability. *Journal of Geophysical Research: Atmospheres*  
1554 112(D12). <https://doi.org/10.1029/2006JD007852>  
1555  
1556 Saji NH, Yamagata T (2003) Possible impacts of Indian Ocean Dipole mode  
1557 events on global climate. *Climate Research* 25(2):151–169. <https://doi.org/10.3354/cr025151>  
1558  
1559 Saji NH, Goswami BN, Vinayachandran PN, et al (1999) A dipole mode in  
1560 the tropical Indian Ocean. *Nature* 401(6751):360–363. <https://doi.org/10.1038/43854>  
1561  
1562  
1563  
1564

- Smith AK (1995) Numerical simulation of global variations of temperature, ozone, and trace species in the stratosphere. *Journal of Geophysical Research: Atmospheres* 100(D1):1253–1269. <https://doi.org/10.1029/94JD02395> 1565  
1566  
1567  
1568  
1569
- Trenberth KE (1980) Planetary Waves at 500 mb in the Southern Hemisphere. *Monthly Weather Review* 108(9):1378–1389. [https://doi.org/10.1175/1520-0493\(1980\)108<1378:PWAMIT>2.0.CO;2](https://doi.org/10.1175/1520-0493(1980)108<1378:PWAMIT>2.0.CO;2) 1570  
1571  
1572  
1573  
1574  
1575  
1576  
1577
- Trenberth KF, Mo KC (1985) Blocking in the Southern Hemisphere. *Monthly Weather Review* 113(1):3–21. [https://doi.org/10.1175/1520-0493\(1985\)113<0003:BITSH>2.0.CO;2](https://doi.org/10.1175/1520-0493(1985)113<0003:BITSH>2.0.CO;2) 1578  
1579  
1580  
1581  
1582  
1583  
1584  
1585
- Turner J, Hosking JS, Bracegirdle TJ, et al (2017) Variability and trends in the Southern Hemisphere high latitude, quasi-stationary planetary waves. *International Journal of Climatology* 37(5):2325–2336. <https://doi.org/10.1002/joc.4848> 1586  
1587  
1588  
1589
- van Loon H, Jenne RL (1972) The zonal harmonic standing waves in the southern hemisphere. *Journal of Geophysical Research* 77(6):992–1003. <https://doi.org/10.1029/JC077i006p00992> 1590  
1591  
1592
- Walker SGT (1914) Correlation in Seasonal Variations of Weather, III: On the Criterion for the Reality of Relationships Or Periodicities. Meteorological Office 1593  
1594  
1595  
1596  
1597  
1598  
1599
- Wickham H (2009) Ggplot2: Elegant Graphics for Data Analysis. Use R!, Springer-Verlag, New York, <https://doi.org/10.1007/978-0-387-98141-3> 1600  
1601  
1602  
1603  
1604
- Wilks D (2011) Statistical Methods in the Atmospheric Sciences, vol 100. Elsevier, <https://doi.org/10.1016/B978-0-12-385022-5.00022-1> 1605  
1606  
1607  
1608  
1609  
1610
- Wilks DS (2016) “The Stippling Shows Statistically Significant Grid Points”: How Research Results are Routinely Overstated and Overinterpreted, and What to Do about It. *Bulletin of the American Meteorological Society* 97(12):2263–2273. <https://doi.org/10.1175/BAMS-D-15-00267.1> 1600  
1601  
1602  
1603  
1604
- Wirth V (1993) Quasi-stationary planetary waves in total ozone and their correlation with lower stratospheric temperature. *Journal of Geophysical Research: Atmospheres* 98(D5):8873–8882. <https://doi.org/10.1029/92JD02820> 1605  
1606  
1607  
1608  
1609  
1610
- Xie P, Arkin PA (1997) Global Precipitation: A 17-Year Monthly Analysis Based on Gauge Observations, Satellite Estimates, and Numerical Model Outputs. *Bull Amer Meteor Soc* 78 (Accessed on <26-08-2021>)(11):2539–2558. [https://doi.org/10.1175/1520-0477\(1997\)078<2539:GPAYMA>2.0.CO;2](https://doi.org/10.1175/1520-0477(1997)078<2539:GPAYMA>2.0.CO;2) 1605  
1606  
1607  
1608  
1609  
1610

36 *SH zonally asymmetric circulation with cEOF*

- 1611 Xie Y (2015) Dynamic Documents with R and Knitr, 2nd edn. Chapman and  
1612 Hall/CRC, Boca Raton, Florida  
1613  
1614 Yu JY, Paek H, Saltzman ES, et al (2015) The early 1990s change in  
1615 ENSO-PSA-SAM relationships and its impact on Southern Hemisphere  
1616 climate. *Journal of Climate* 28(23):9393–9408. <https://doi.org/10.1175/JCLI-D-15-0335.1>  
1617  
1618  
1619  
1620  
1621  
1622  
1623  
1624  
1625  
1626  
1627  
1628  
1629  
1630  
1631  
1632  
1633  
1634  
1635  
1636  
1637  
1638  
1639  
1640  
1641  
1642  
1643  
1644  
1645  
1646  
1647  
1648  
1649  
1650  
1651  
1652  
1653  
1654  
1655  
1656